Master's Thesis

Mineralogical deportment and Trace Element Geochemistry of REEs in the Blötberget Apatite-Iron-Oxide Deposit, Central Sweden

Léopold Chicoine
2025

Degree Project in Geology 45 hp

Master of Earth Sciences, Department of Earth Sciences, University of Gothenburg

UNIVERSITY OF GOTHENBURG

Abstract

This study employed a multi-analytical approach, combining Nordic Iron rare earth element (REE) data on a meter scale with Minalyze (Veracio) drill core scanner data on a millimetre scale, to identify the most enriched REE zones in the Blötberget iron oxide-apatite (IOA) deposit. The goal was to develop and apply a new method for identifying REE-enriched samples and extracting more information from existing, poorly constrained data, while reducing sampling time and improving cost efficiency. Three drill cores were sampled: one from the hanging wall, one from the footwall, and one from the iron ore, to investigate REE-hosting phases, textures, and compositional variations across the mineralised zones using X-ray fluorescence, SEM, and LA-ICP-MS. The results show significantly higher concentrations of heavy rare earth elements (HREEs) in apatite but lower light rare earth element (LREE) contents compared to those commonly reported in other Kiruna-type deposits. Clear compositional and textural differences exist between the structural domains: the footwall is dominated by allanite, a refractory REE host, while the hanging wall contains free-milling monazite and xenotime occurring as large, isolated grains. Apatite in the hanging wall is enriched in both LREE and HREE, including the highest HREE values measured, whereas footwall apatite is comparatively LREE-depleted. Eu anomalies support derivation from separate magma batches, with the footwall representing a more evolved intrusive protolith and the hanging wall a less evolved, subvolcanic equivalent. Textural evidence indicates that monazite postdates apatite, with apatite locally breaking down to form secondary REE phases during a late magmatic to hydrothermal stage. This remobilisation locally enriched the host rocks without obliterating the magmatic signature. By analogy with Kiruna, where secondary monazite and xenotime formed during multiple hydrothermal pulses between ~1.9 and 1.5 Ga, Blötberget may also preserve evidence of a prolonged or episodic hydrothermal history. From an economic perspective, the mineralogical contrast has direct implications: the hanging wall, with free-milling monazite and xenotime, is more favourable for REE extraction, whereas the allanite-rich footwall poses challenges for processing. Apatite across all zones is relatively low in deleterious elements compared to other IOAs, enhancing its potential as a phosphorus byproduct source. A comprehensive and unbiased core scan of Blötberget is recommended to evaluate whether the observed REE enrichments and mineralogical variations are localised features or representative of broader zones, and geochronological dating of monazite and xenotime will be critical to constrain the timing of REE enrichment relative to iron ore formation.

Contents

1. Introduction

1.1 Iron Mining History of Sweden

Sweden's iron ore mining began around 2700 BCE in central regions such as Bergslagen, where limonite-rich bog iron ore was first smelted. Over time, it evolved in response to increasing demand for larger and deeper ore deposits to support industrial-scale mining. As a result, the Dannemora iron mine, located near Uppsala, was one of Europe's most important iron mines in the 17th and 19th centuries. The Grängesberg iron mine was Sweden's largest iron ore producer until the 20th century, when Kiruna and Malmberget became the primary suppliers of iron ore, and Grängesberg closed. Sweden's iron exports from Bergslagen were already significant during the Middle Ages, supplying early blast furnaces and forming the foundation of the Swedish steel industry, which remains central today opening of Kiruna and Malmberget in the late 19th century marked a transition from smaller, high-grade Bergslagen mines to large-scale mechanised operations in Norrbotten, consolidating Sweden's role as a leading iron supplier in Europe (Geijer & Magnusson, 1944; Magnusson, 1970; Tegengren, 1924).

The Blötberget mine, located in the Bergslagen District, was historically mined for its high-grade magnetite ore until 1979. Since 2007, new exploration activities have been undertaken in the area to reopen the mine. Nordic Iron received the necessary licenses to exploit iron oxides, lanthanoids, and apatite in 2011 and the environmental license in 2014. In 2015 and 2016, laboratory and pilot-scale metallurgical beneficiation optimisation tests demonstrated that the raw ore could be beneficiated to an ore concentrate with an iron content of 69%, an extremely high amount, resulting in a high-purity product suitable for iron production by direct reduction. The Blötberget resources at a COG of 25% Fe are 55.1 Mt at a grade of 40.7 % Fe no Total) and 0.5 % P (Nordic Iron, 2017). Historically, the mining was done at a shallow level (~240 m) and targeted the most accessible and high-grade zones. Nordic Iron plans to increase the depth of its operations to 420 meters (Nordic Iron, 2025). Unlike Kiruna and Malmberget, the apatite-rich ores of Blötberget and Grängesberg also contain appreciable phosphorus and rare earth elements, making them potential future sources of critical raw materials in addition to iron. Renewed exploration in Bergslagen, therefore, reflects not only interest in high-purity magnetite but also in phosphorus and REE by-products, aligning with European critical raw material strategies (Jonsson et al., 2016; Nordic Iron Ore, 2017).

1.2 Geological Setting

1.2.1 Geology and tectonic evolution of Blötberget

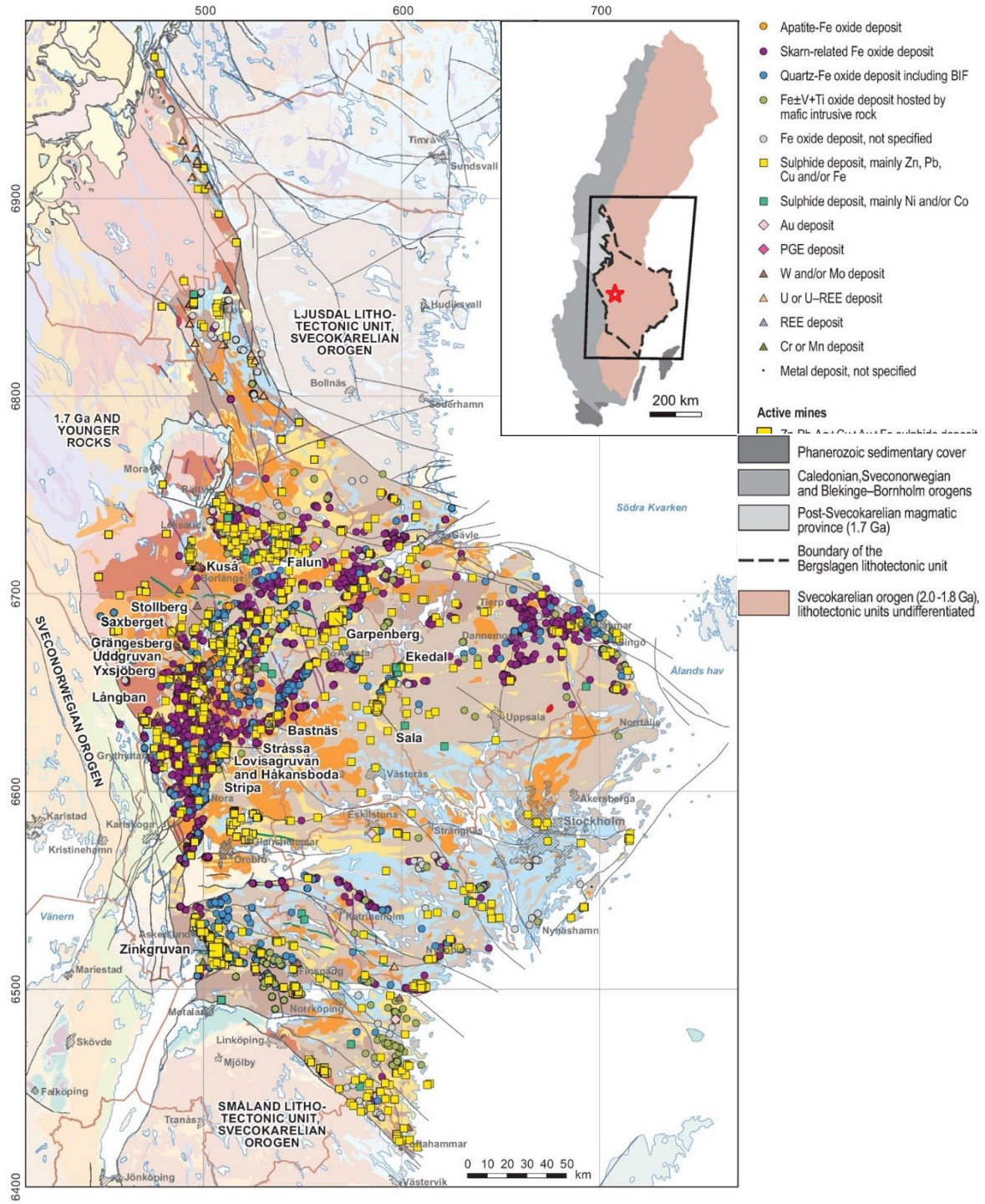

Figure 1. Distribution of metallic mineral deposits in the Bergslagen lithotectonic unit and adjacent areas, categorised by commodities. Operating mines are marked with larger symbols, key deposits in bold. Maps of operating mines follow. Data from the Geological Survey of Sweden; background geology from Fig. 6.2. Deposits near Loftahammar and Karlskoga extend into the Småland unit and the Sveconorwegian orogen. BIF, banded iron formation; PGE, platinum group elements; REE, (M. Stephens & Jansson, 2020).

The Blötberget deposit is a part of the Bergslagen district, which underwent multiple phases of metamorphism and deformation related to the Svecokarelian orogeny (1.9–1.8 Ga). These

tectonothermal events led to the complex folding, faulting, and reworking of the iron ores under amphibolite-facies metamorphic conditions. The Bergslagen crust is interpreted to have formed in a Paleoproterozoic magmatic arc setting, with juvenile and reworked continental crust contributing to a long-lived active margin environment (M. B. Stephens et al., 2009). The Blötberget deposit includes three ore bodies: Hugget-Flygruvan, Sandellmalmen, and Kalvgruvan. They have been interpreted as Kiruna-type IOA deposits that were subjected to intense deformation, interbedded with Proterozoic metavolcanic and metasedimentary rocks typical of the Bergslagen mining district (Andersson et al., 2006; Jansson & Allen, 2011). The high-grade Kiruna-type iron ore deposits mined in northern Sweden constitute the primary domestic source of iron in the European Union (Hitzman et al., 1992; Jonsson et al., 2013). These deposits are associated with felsic to intermediate metavolcanic rocks, often intruding granitic plutons. These deposits are rich in phosphorus-bearing minerals and show REE enrichment, mainly hosted in fluorapatite but also present in monazite, xenotime, and allanite (Jonsson et al., 2013, 2016). The REE and phosphorus enrichment in Kiruna-type systems such as Blötberget likely reflects the behaviour of incompatible elements during both magmatic and hydrothermal stages, with apatite being the primary host. However, REE enrichment alone does not indicate a specific origin, since it can result from early magmatic crystallisation or later hydrothermal remobilisation. At Blötberget, the presence of biotite and amphibole near the ore bodies, along with elevated Mg and K, points to localised hydrothermal alteration linked to the iron oxides (Jiao, 2011). Magnetite-hematite-apatite ores in Kiruna-type systems typically contain 0.05–5% P and are enriched in REEs (Parak, 1975; Wanhainen et al., 2017). The Grängesberg magnetite-hematite-apatite ores contain fluorapatite enriched in REE oxides up to 2–3 wt.%, with accessory phases such as allanite, forming in fractures, crack fillings, and late-stage hydrothermal veins (Jonsson et al., 2016).

1.2.2 Iron oxide-apatite deposits

IOA deposits are massive to banded rocks rich in magnetite and/or hematite, often showing coarse-grained textures. They commonly occur within intermediate to felsic volcanic or subvolcanic rocks. “Kiruna-type” IOA deposits will be considered in this study as a subtype, characterised by magnetite ore containing 5–15 wt.% fluorapatite and enriched in uranium and REEs (Reich et al., 2022; Rojas et al., 2018). The origin of these deposits is a topic of ongoing debate between magmatic and hydrothermal models. Oxygen isotope data from deposits such as Grängesberg and Kiruna align with high-temperature formation conditions. While these signatures cannot fully distinguish between magmatic and high-temperature hydrothermal (Henriksson, Troll, Kooijman, Bindeman, Naeraa, Bauer, et al., 2024) processes, they suggest a predominantly magmatic origin with only minor later fluid overprint (Jonsson et al., 2013; Troll et al., 2019). Further support comes from Kiruna and Malmberget, where magnetite textures and element patterns indicate crystallisation directly from magma In contrast, a purely hydrothermal model posits that IOA deposits formed primarily through Fe-rich fluids circulating through the crust, leaching iron from protoliths, and precipitating magnetite. Evidence cited for this model includes widespread alteration halos (e.g., scapolitization, K-metasomatism) and breccia or vein-style magnetite (Hitzman et al., 1992; Nystroem & Henriquez, 1994). However, these models cannot easily explain the high-temperature isotopic signatures, magmatic textures, or the enormous fluid volumes that would be required. A more widely accepted explanation is a magmatic–hydrothermal framework, in which IOA deposits originate from subduction-related, water-rich, and chlorine-rich intermediate magmas. As these magmas evolve, both direct igneous crystallisation of magnetite and the exsolution of volatile-rich fluids contribute to ore formation. The fluids efficiently scavenge iron from the melt and

precipitate magnetite across a broad temperature spectrum (~1,000 to 300 °C). Concentration of magnetite in the upper crust is therefore linked to a combination of igneous crystallisation, volatile exsolution, and the focused transport of Fe-rich fluids under extensional tectonic conditions (Henriksson et al., 2024; Wang et al., 2021).

1.3 Rare Earth Elements and Associated Minerals

1.3.1 Rare Earth Elements

The rare earth elements (REEs) form a group that includes the 15 lanthanoids, coupled with scandium (Z=21) and yttrium (Z=39), due to their chemical similarities. Scandium is not discussed further in this study. It is commonly accepted that REEs are divided into two main categories: the light REEs (LREE), which include lanthanum (La), cerium (Ce), praseodymium (Pr), neodymium (Nd), promethium (Pm), samarium (Sm), and europium (Eu), and the heavy REEs (HREE), which include yttrium (Y), gadolinium (Gd), terbium (Tb), dysprosium (Dy), holmium (Ho), erbium (Er), thulium (Tm), ytterbium (Yb), and lutetium (Lu) (Henderson, 1984). Yttrium was first described in 1794 by Johan Gadolin, a Finnish chemist who analysed a rock from Ytterby. It became the first rare earth-like element to be identified by isolating an impure mixture of heavy rare earth oxides that was named yttria from the mineral gadolinite (Gadolin, 1794; Weeks & Leicester, 1968). Lutetium was the last of the naturally occurring REEs to be discovered in 1907 in gadolinite (Urbain, 1907). Their similar geochemical behavior can explain the lengthy time frame needed for the identification of all 17 REE: they are typically associated with one another in nature, they are lithophile oxides commonly found in the Earth's crust, and they predominantly occur in the trivalent oxidation state with similar ionic radii, from around 106 picometers (pm) for lanthanum to around 85 pm for lutetium. However, these values vary depending on coordination number; for example, lanthanoids exhibit different radii in 6-fold coordination, as in monazite, compared to 8-fold coordination, as in xenotime. Exceptions include Eu^{2+} (117 pm) and Ce^{4+} (87 pm), which occur in reducing and oxidising environments, respectively. Although not particularly rare in crustal rocks, REEs usually occur in low concentrations, substituting into the crystal lattices of other minerals and rarely forming primary phases, which makes them notoriously difficult to separate (Shannon, 1976; Shannon & Prewitt, 1969). Their recent surge in popularity among other metallic elements in the periodic table is attributed to their application in high-tech, especially in the development of new technologies, and their key role in accelerating the energy transition. This is especially true for Pr, Nd, Tb, and Dy, which are critical for high-performance magnets used in wind turbines and electric vehicle motors. Their usage is 91% due to the demand for low-carbon emission energies (Renas Sidahmed, 2023; Windfakten, 2024). Currently, no REE mine is operational in the European Union. This creates a considerable supply risk in the context of trade wars and lockdowns, which could make Europe unable to obtain those critical materials. The European Raw Materials Alliance (ERMA) released in 2021 an action plan to increase the pace of funding for REE projects to lessen the dependence on China and Russia, which supplied 74.7% of its REE imports in 2023, which were 6,000 and 3,700 tons, respectively (European Raw Materials Alliance, 2021; Eurostat, 2025). Although no REE mines are currently active in Europe, the continent has a strong historical connection to these elements. Many of these elements were first discovered in minerals from Ytterby and Bastnäs in Sweden. Ongoing projects, such as Norra Kärr, which is rich in HREEs, aim to create a domestic supply and reduce reliance on imports (Leading Edge Materials, 2021). A compilation of prominent REE projects in Europe and Greenland is shown in Table 1. Production of REEs and estimated reserves are listed in Table 2.

	Company	Location	Deposit type	REE mineral	Total Resource (Mt)	Grade (wt.% TREO)	HREE percentage
Tanbreez	Tanbreez Mining Greenland	Greenland	Alkaline rock	Eudialyte	2900	0.617	31.0%
Kvanefjeld	Minerals Limited Greenland	Greenland	Alkaline rock	Steenstrupine-(Ce)	1114	1.1	11.6%
Lovozersky	LLC Lovozersky GOK	Russia	Alkaline rock	Loparite	717	1.12	4.45%
Fen	REE Minerals Holding AS	Norway	Carbonatite	Bastnäsite	462	2.15	1.60%
Norra Kärr	Leading Edge Materials Corp	Sweden	Alkaline rock	Eudialyte	110	0.59	52.0%
Per Geijer	LKAB	Kiruna, Sweden	Iron-Phosphate-Apatite	Apatite	734	0.18	17%
Korsnäs	Prospech Ltd.	Finland	Carbonatite	Monazite	0.87 (mined)	0.7-2.2	2-9

Table 1. Prominent REE exploration projects in Europe and Greenland.*(A. Lindberg, 2023; Goodenough et al., 2016; J. Edwards, 2023; Leading Edge Materials, 2021; Strategic Metals Invest, 2025)*

	Production 2023 (tonnes)	Production 2024 (tonnes)	Reserves
China	255000	270000	44000000
Brazil	140	20	21000000
Australia	16000	13000	15700000
India	2900	2,900	6900000
Russia	2500	2500	3800000
Vietnam	300	300	3500000
United States	41600	45000	1900000
Greenland	-	-	1500000
Tanzania	-	-	890000
South Africa	-	-	860000
Canada	-	-	830000
Thailand	3600	13000	4500
Burma	43000	31000	NA
Madagascar	22100	2000	NA
Malaysia	310	130	NA
Nigeria	7200	13000	NA
Other	1,440	1100	NA
World total (rounded)	376000	390000	>90000000

Table 2. World mine production and reserves, including those of Russia, South Africa, the United States, and Vietnam, were updated based on reports from companies and governments. (U.S. Geological Survey, 2025).

1.3.2 Apatite

Apatite is Earth's most abundant natural phosphate; it plays a critical role in the global phosphorus cycle and serves as its primary commercial source (Hughes & Rakovan, 2002). Unlike nitrogen, phosphorus is a limiting nutrient for terrestrial biological productivity. It is rare in the Earth's crust and is moved only by water from land to sea, where it is sedimented on continental margins, remaining there until it is subducted. The primary source of phosphorus-bearing minerals in igneous rocks is fluorapatite, which occurs as small accessory grains. Sedimentary rocks often contain carbonate-fluorapatite (CFA), formed in situ (Filippelli, 2008). This mineral is also key in IOA deposits, which are significant for iron and phosphorus, and can contain variable amounts of REEs (Troll et al., 2019). Apatite is a diverse mineral group with a versatile atomic structure capable of incorporating nearly half of the periodic table's elements (Hughes & Rakovan, 2015). Its generic formula is: $A_5(XO_4)_3Z$ (Pan & Fleet, 2002; Piccoli & Candela, 2002). In its crystallography, the (XO_4) site typically hosts phosphate (PO_4^{3-}) but can also accommodate arsenate, vanadate, and other anion groups (e.g., AsO_4^{3-}, VO_4^{3-}, SO_4^{3-}). The (Z) site is commonly occupied by F−, Cl−, or OH−, which define fluorapatite, chlorapatite, and hydroxyapatite, respectively. Fluorapatite is the most common, but natural varieties often include some Cl− and OH−. The (A) site is predominantly Ca^{2+}, but can be substituted by various divalent (e.g., Sr^{2+}, Pb^{2+}), monovalent (Na^{+}), trivalent (REE^{3+}), and tetravalent (Th^{4+}, U^{4+}) cations. Sr^{2+} is the most common substituent (Hughes & Rakovan, 2015; Pan & Fleet, 2002). Apatite can contain substantial REE quantities, ranging from thousands of ppm to several weight per cent, making it an essential element for quantitative analysis of REE content in igneous rocks. Specific substitution schemes often balance REE enrichment (Ptáček, 2016; Rønsbo, 2008).

$$Ca^{2+} + P^{5+} = REE^{3+} + Si^{4+}$$

$$2\ Ca^{2+} = Na^{+} + REE^{3+}$$

1.3.3 Rare Earth Minerals

While over 200 minerals are known to contain REEs, only a select few are economically significant sources. These include phosphates such as monazite and xenotime, carbonates such as bastnäsite and synchysite, and complex silicates like allanite and eudialyte (Dostal, 2017; Jackson & Christiansen, 1993; Rasool et al., 2025). In IOA deposits, REEs are commonly associated with and often incorporated within the crystal structure of apatite. While apatite is the primary host, it contains a limited amount of REEs, thus it is not preferred as a primary source for economical extraction (Bonyadi et al., 2011). REE-bearing minerals are present in varying amounts, monazite [(Ce,La,Nd,Th)(PO_4)], and allanite [(Ce, Ca,Y)(Al,Fe^{2+}, Fe^{3+})$_3$(SiO_4)$_3$(OH)], contribute to the overall LREE budget of the deposit. In contrast, xenotime YPO_4 contributes to the concentration of HREEs in the deposit. The specific assemblage and relative abundance of these minerals determine the REE distribution and influence potential extraction methods. (Kanazawa & Kamitani, 2006; Khoshnoodi et al., 2023). Ion-adsorption clay is the most preferable option since the REEs are exchangeable and liberated in soft clays, and do not occur in minerals, which lowers processing costs. They can be leached off with mild ammonium sulfate or similar weak solutions at room temperature (Moldoveanu & Papangelakis, 2016). Carbonatite and igneous rocks possess high REE concentrations but are challenging to process due to the radioactivity of monazite and their more complex mineralogy (Chen et al., 2017).

Regolith-hosted weathering crust on granite is shallow and abundant, making it economical despite its low grade (Borst et al., 2020).

Eudialyte-hosted REE deposits, such as Norra Kärr, are considered the most challenging deposits to extract due to the REEs being locked in a complex silicate lattice that is chemically resistant, requiring high-temperature, multi-step acid or alkali processing and generating large volumes of waste. Their highly elevated HREE grade makes them economically viable. Table 3 lists the major REE-bearing minerals that can be found in REE deposits.

Mineral	**Formula**	**Approx. REO %**
Apatite	$(Ca,Ce)_5(PO_4)_3(F,Cl,OH)$	19
Euxenite-(Y)	$(Y,Ca,Ce,U,Th)(Nb,Ta,Ti)_2O_6$	24
Samarskite-(Y)	$(Y,Ce,U,Fe^{3+})_3(Nb,Ta,Ti)_5O_{16}$	24
Loparite	$(Ce,La,Na,Ca,Sr)(Ti,Nb)O_3$	30
Aeschynite-(Ce)	$(Ce,Ca,Fe,Th)(Ti,Nb)_2(O,OH)_6$	32
Britholite-(Ce)	$(Ce,Ca)_5(SiO_4,PO_3)_3(OH,F)$	32
Cebaite-(Ce)	$Ba_3Ce_2(CO_3)_5F_2$	32
Florencite-(Ce)	$CeAl_3(PO_4)_2(OH)_6$	32
Allanite-(Ce)	$(Ce,Ca,Y)(Al,Fe^{3+})_3(SiO_4)_3OH$	38
Huanghoite-(Ce)	$BaCe(CO_3)_2F$	39
Synchysite-(Ce)	$Ca(Ce,La)(CO_3)_2F$	51
Fergusonite-(Ce)	$(Ce,La,Nd)NbO_4$	53
Yttrocerite	$(Ca,Ce,Y,La)F_2{\cdot}nH_2O$	53
Kainosite-(Y)	$Ca_2(Y,Ce)_2Si_4O_{12}CO_3{\cdot}H_2O$	38
Gadolinite-(Ce)	$(Ce,La,Nd,Y)_2Fe^{2+}Be_2Si_2O_{10}$	60

Mineral	Formula	Approx. REO %
Parisite-(Ce)	$Ca(Ce,La)_2(CO_3)_3F_2$	61
Xenotime	YPO_4	61
Monazite-(Ce)	$(Ce,La,Nd,Th)PO_4$	65
Bastnäsite-(Ce)	$(Ce,La)(CO_3)F$	75
Brannerite	$(U,Ca,Y,Ce)(Ti,Fe)_2O_6$	9
Eudialyte	$Na(Ca,Ce)_2(Fe^{2+},Mn,Y)ZrSi_8O_{22}(OH,Cl)_2$	1-10
Knopite	$(Ca,Ti,Ce_2)O_3$	N/A

Table 3. List of typical REE-bearing minerals phases and their molecular formulas, and typical values of their rare earth oxide (REO) contents. *(Kanazawa & Kamitani, 2006, M. Borst et al., 2019)*

1.3.4 Nordic Iron Rare Earth Minerals

During the 2023 Blötberget sampling campaign, Nordic Iron initiated a resampling of existing drill cores to evaluate the presence and distribution of REEs within the deposit. The cores were re-logged and analysed by the company ALS, with significant elements measured by X-ray fluorescence (XRF) and trace elements, including REEs, quantified using inductively coupled plasma mass spectrometry (ICP-MS). This approach aimed to enhance the geochemical understanding of REE occurrences in relation to iron-apatite mineralisation and to assess their potential economic significance within the broader context of the deposit. The results of the assays showed 6,574 ppm total REE in the footwall contact, and 876 ppm in the main ore body, alongside 1,127 ppm in the tailing samples from five samples (Nordic Iron, 2023). A follow-up campaign in autumn 2023 confirmed these results and highlighted even higher concentrations. Those drill cores showed total REE (TREE) concentrations reaching up to 15,285 ppm (1.53%) in the hanging wall, 1,167 ppm in the ore body, and an average of 1,127 ppm in tailing samples, based on five analyses. Notably, neodymium, praseodymium, and dysprosium constitute 21% of the TREE grade. These results confirmed the presence of elevated concentrations of REE in parts of the Blötberget iron ore deposit. They presented a potential economic viability of extracting REEs such as neodymium and praseodymium. (Nordic Iron, 2023). While promising, the REE grades need confirmation through broader sampling and mineralogical characterisation. The limited knowledge about the host minerals and the REE content in apatite was the leading motivation for this thesis work.

1.4 Aim of this study

This thesis aims to contribute to the evaluation of a potential by-product of phosphorus and REE from the planned iron ore production. This study is based on elemental deportment and textural characteristics of mineralisation. An innovative multi-step evaluation is implemented and detailed in the methodology section.

The goals of the study are to:
1. Determine the distribution of REE in mineralised drill core sections and their association with other chemical elements.
2. Describe the minerals that host REE in mineralised drill core sections and characterise their textural relations to other minerals, including iron oxides and gangue.
3. Assess the chemical composition of REE- and P-bearing minerals.
4. Synthesise the mineralogical and geochemical data in the context of the potential for extraction of P and REE in a possible by-product stream to iron ore mining.

2. Materials & Methods

2.1 Drill core samples

Drill cores recovered from drillings are kept in boxes marked according to the project, the year, the drill hole, and the core box:

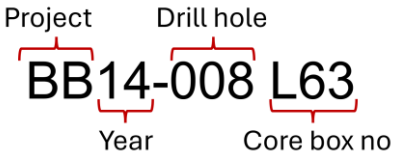

One of the many issues with REE minerals is the visual identification of REE enrichments, which is not feasible because REE-bearing minerals are typically indistinguishable from others. Consequently, alternative analytical methods such as XRF and ICP-MS are required. Nordic Iron employed the analytical techniques of ALS. Following analysis by ALS using XRF and ICP-MS, Excel data sheets containing major, trace, and REE concentrations were provided by Nordic Iron for this study. Access to these sheets allowed the creation of scatter plots to identify correlations between major elements and REEs. The data showed that drill cores BB_14-001 (386.98–583.55 m) and BB_14-008 (341.21–414.94 m) contained the most significant REE enrichment. Since the deposit is of the IOA type, where REEs are commonly hosted in phosphate minerals such as apatite and potentially monazite, phosphorus was used as a proxy for REE-bearing phases. A positive correlation was observed between P and total REE content. The highest P value was 6.70 wt.% for 6574 ppm REE at 393.25 m in BB_14-001, followed by 2.91 wt.% P for 15,285 ppm REE at 345.77 m. BB_14-008 L63 represents the hanging wall, and BB_14-001 L71 is the footwall, with the hanging wall lying above the ore body and the footwall below. Figure 2 provides a visualisation of the current geological model Nordic Iron is using to predict the location of the iron mineralisation.

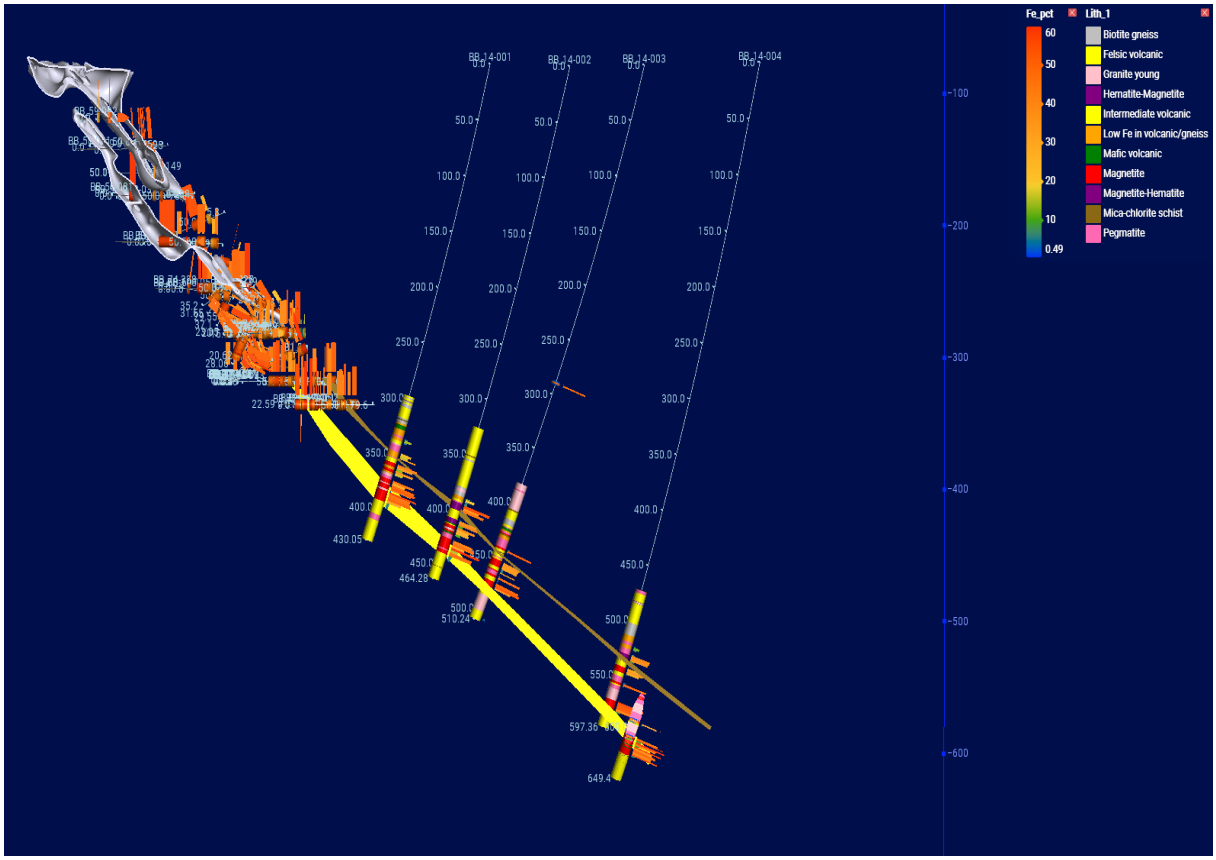

Figure 2a. 3D geological model of the Blötberget IOA deposit. The model displays four drill holes, including BB14-001.

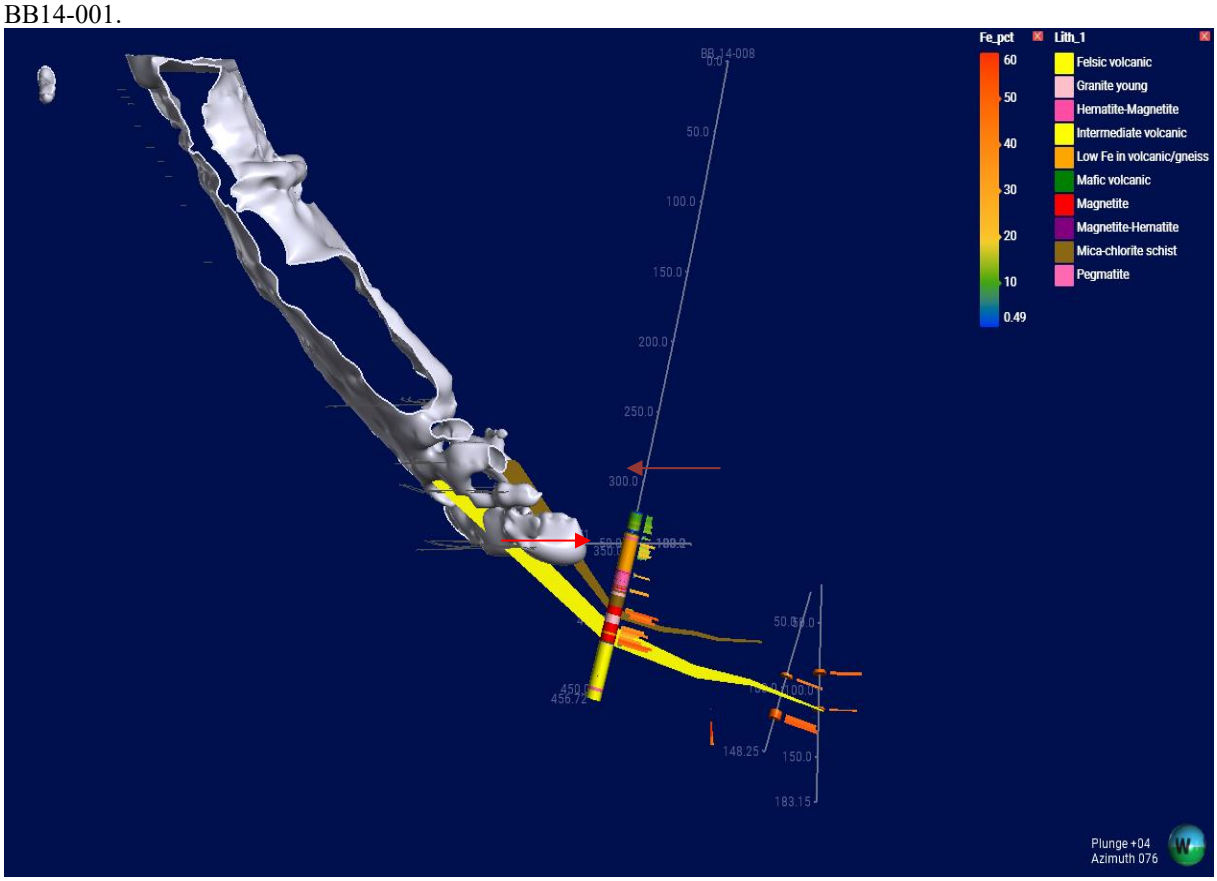

Figure 2b. 3D geological model of the Blötberget IOA deposit. Ore bodies are shown in white, and drill holes are coloured by Fe content (from <1% in blue to >60% in red) and lithology, as indicated in the legend. Yellow sheet-like volumes represent high-grade (Model provided by Nordic Iron).

Sampling of the drill cores was intentionally biased toward zones already identified as enriched in REEs, P, Ca, and Ti. Therefore, the dataset does not allow for an unbiased assessment of REE distribution across the entire Blötberget deposit. These samples are not intended to be representative of the whole deposit but were specifically chosen to study the processes that formed them. The sampled core sections were taken from mineralised intervals and placed in core boxes, which Nordic Iron loaned to the University of Gothenburg for this project.

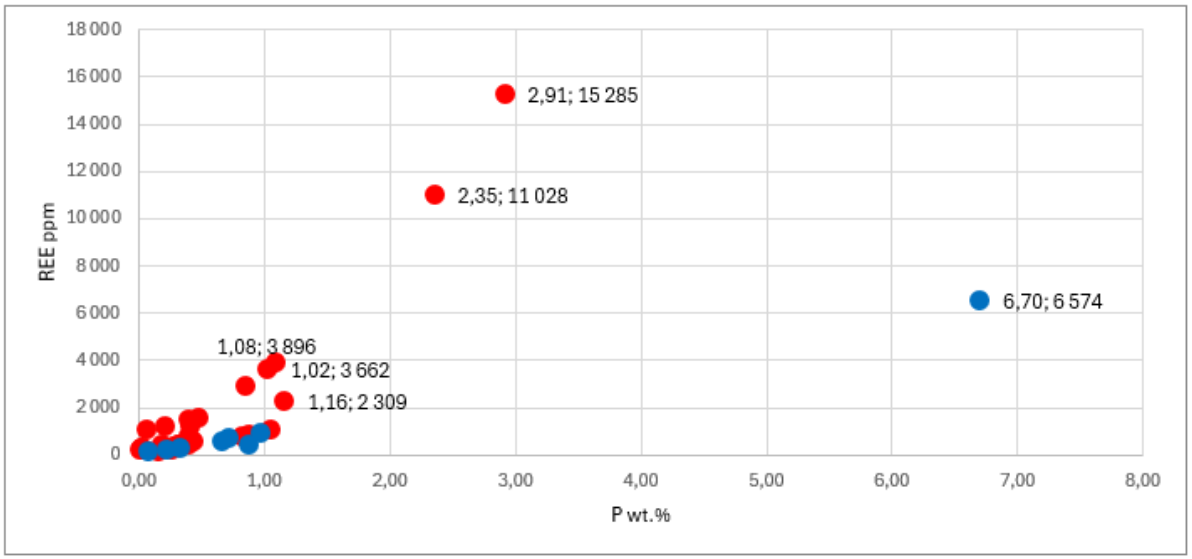

Figure 3. Scatter plot showing the correlation between P in wt.% and REE concentrations in ppm in selected intervals from drill cores BB_14-001 and BB_14-008 at Blötberget. Phosphorus was used as a proxy for apatite abundance, the primary REE-hosting phase in IOA deposits. Data shows a positive correlation, supporting apatite as the potential leading carrier of REEs in the sampled mineralised zones.

Three parts of the drill core are distinguished in Figure 4. The black zone, identified as iron ore, is composed of magnetite and hematite and displays a heterogeneous texture with lighter white to grey interstitial material, indicating variations in iron content and possibly late-stage hydrothermal alteration. The footwall, which resembles the iron ore, is fine-grained and slightly mesocratic, with a more greyish tone, which is likely due to its high silicon content. The hanging wall is more leucocratic, dominated by felsic phases, marked by black magnetic spots, and crosscut by an orange to pink crystalline vein. Similar colouration appears at several other locations within the drill core, suggesting repeated late-stage hydrothermal quartz-feldspar intrusions.

Figure 4. Drill core images created by the Minalyzer CS.

2.2 High-resolution XRF scanning

Since the REE mineralisation is “invisible” to the eye, the 2-metre-long drill core samples were brought to Minalyze (Veracio) to obtain 1-centimetre-resolution continuous X-ray fluorescence data, in addition to colour photographs to evaluate the distribution of REE and other chemical elements within the sections of core. The core scanner Minalyzer CS is designed to scan drill cores directly in the core trays. A LiDAR system generates a 3D model of the topography of the core and trays, allowing the X-ray detector to maintain a consistent distance for precise scanning. The user will obtain a high-resolution elemental profile path of the drill core with a 1-centimetre resolution of the scans (Intertek, 2025). The pXRF and Minalyzer CS operate on the same principle: they excite atoms to produce a spectrogram of the elemental composition. The Minalyzer CS is a more complex stand-alone instrument that collects chemical analyses of drill cores through X-ray fluorescence (XRF) using energy-dispersive spectroscopy (EDS) with a silicon drift detector (SDD). This principle enables quick analysis and facilitates continuous and rapid data acquisition. Helium flow is used to displace air and improve sensitivity to light elements.

Figure 5. Minalyzer CS (Chalmers Ventures, 2018).

The scans can be carried out with different X-ray tube voltages up to 50 kilovolts (kV). Different voltages will allow for detecting elements across a wider atomic range, with low voltage suitable for lighter elements (e.g., Al, Si, P), and high voltage for heavier elements (e.g., REEs, Pb, U). The tube current, expressed in milliamperes (mA), regulates the intensity of the X-ray beam; higher currents produce a stronger signal and greater sensitivity. Despite the beam's intensity, the drill cores remain undamaged due to the non-destructive nature of the analysis. X-ray tubes are enclosed in a radiation-shielded housing to ensure user safety. Choosing three voltages creates three scans, allowing for more accurate results depending on the desired elements. The X-ray beam location and intensity are verified throughout the entire scanning process and logged to monitor potential instrument drift. Calibrations and drift corrections were performed using matrix-matched certified reference materials (e.g., apatite, basalt standards) and blank samples. This ensures the availability of important components during analytical campaigns, thereby supporting QA/QC routines. The operator corrects and uploads the data to Veracio's server, which users can access via the website *Minalogger.com*. The platform offers a comprehensive elemental table and a complete visual representation of the scanned drill cores. Scan results are displayed as a colour gradient (green for the lowest to red for the highest concentrations) on *Minalogger.com*, showing the elemental distributions across the drill core in counts per second and providing insight into where to sample the core.

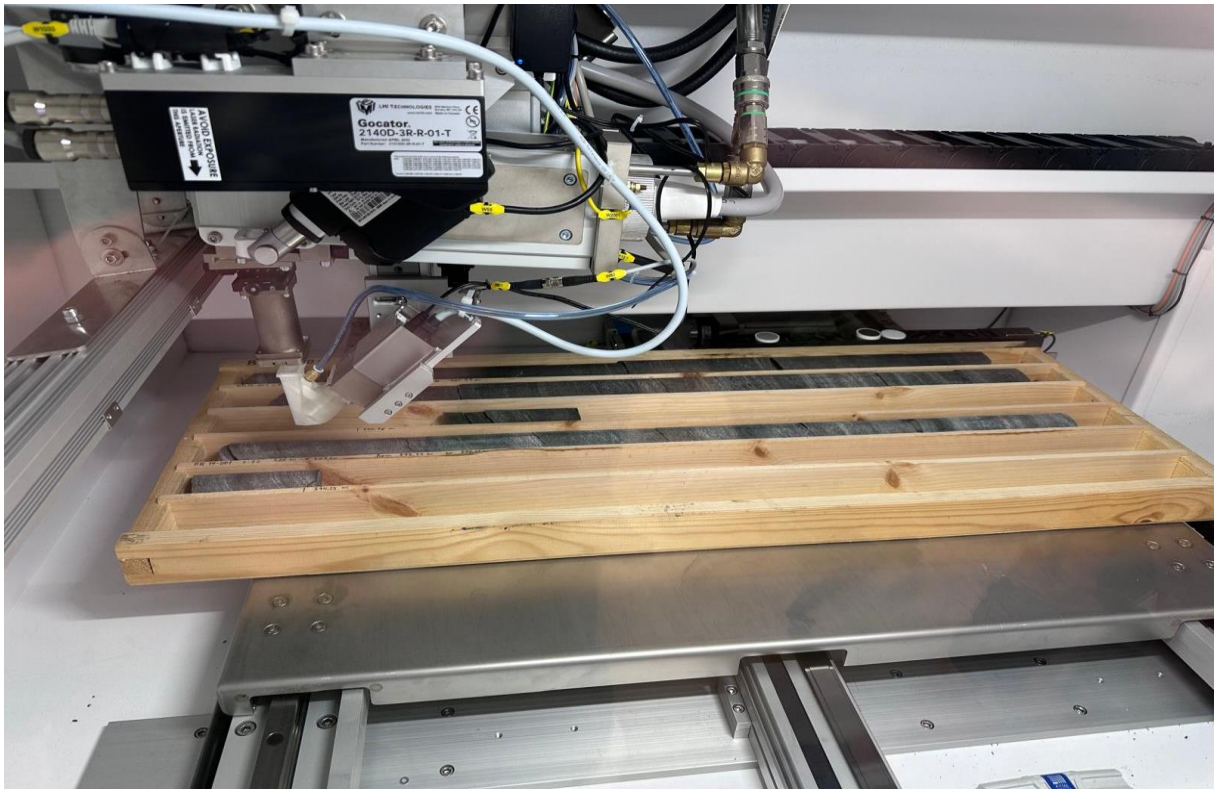

Figure 6. Minalyzer CS in action (picture by the author).

2.2.1 Scan Settings

To improve resolution and signal quality, the scans were carried out using the slowest setting of 1 mm per second. Since Blötberget IOA hosts significant phosphorus, shows potential REE enrichment, and deleterious elements are of interest (e.g., U, Pb, As), three voltage settings of 15, 30, and 50 kV were used to detect both light and heavy elements. The scans were conducted at 18 mA to maximise signal strength and sensitivity. Each scan took approximately 45 minutes, so a total of two hours was necessary to complete all three scans. The 50 kV option was used to detect areas with the highest concentrations of REEs, especially Ce, La, and Y, which are among the more accurately detected REEs; the 30 kV option was used for iron (Fe) and Titanium (Ti), and the 15 kV setting was used to detect lighter elements such as Phosphorus (P). This method enabled the precise identification of sections within the drill cores containing elevated concentrations of specific elements, and helped select small, targeted intervals for cutting. High-value zones were, in general, chosen to facilitate the process of finding rare earth-bearing minerals during SEM analysis; however, random, depleted areas were also sampled to ensure a representative overview of the iron ore and the surrounding mineralisation. Eleven samples were taken: four from the iron ore, two from the footwall, and five from the hanging wall. P, Ca, Ce, Y, Fe, and Ti were used as key elements for sample selection. This choice was based on the established knowledge that the samples originate from a Kiruna-type IOA deposit. The presence of apatite typically indicates elevated levels of phosphorus and calcium. As mentioned earlier, cerium and lanthanum are commonly associated with LREE-bearing minerals, such as monazite, while yttrium serves as a reliable indicator for HREE-bearing minerals, such as xenotime (YPO_4). Ti-bearing minerals are refractory in both iron and apatite processing, making it important to identify the minerals in which titanium is hosted. Moreover, the correlation between Ti and P content could provide insights into the geochemical behaviour and processing challenges of mineralisation (Belousova et al., 2002a).

2.3 Scanning electron microscope

Scanning electron microscopy (SEM) was the primary instrument used in this project. All quantitative analyses and backscattered electron (BSE) imaging were conducted using a JEOL NeoScope JCM-7000 benchtop SEM at the University of Gothenburg, operated at a landing voltage of 15 kV, a beam current of 20 nA, high probe current (High-PC), and under high-vacuum conditions. Dwell time varies between 15 and 60 seconds, depending on the objective. REE-bearing and exotic minerals were analysed with longer dwell times, while more common minerals were measured with shorter dwell times. EDS spectra were used to determine mineral phases within samples, whereas backscatter electron (BSE) images were used to obtain detailed textural knowledge. The primary groundmass of minerals and REE-bearing phases in the samples was analysed through SEM, and then elemental maps were made for LA-ICP-MS analysis. An emphasis was put on examining the textural and spatial relationships between groundmass minerals and REE minerals. While epoxy mounting is typically used to stabilise samples for SEM and LA-ICP-MS analyses, only one sample in this study was mounted in epoxy (4.16 g epoxy, 0.5 g hardener). It was quickly found that this approach was deemed unnecessary for the remaining samples, as the drill core material was clean and precisely cut to fit the SEM holder without additional support. Using a diamond saw allowed for smooth cuts and exposed a larger surface area for observation, whereas epoxy-mounted samples require extra space for the surrounding resin. As a result, all but one sample were analysed without epoxy, improving analytical results by reducing contamination-related C, O, N, and Cl peaks while enhancing surface visibility. All the samples were carefully numbered and polished down to 0,04 μm with colloidal silica. Once polished, a fine layer of carbon was applied to every puck to make the samples electrically conductive and prevent charging during SEM imaging and analysis. Added carbon must be accounted for and subtracted since it can potentially skew the atom% calculations and affect the determination of mineral compositions. Once put in the SEM puck holder, a line of copper was connected, touching the coating, and the puck holder provided a path for electrons to dissipate, ensuring a stable image and accurate results from the SEM analysis.

2.3.1 ImageJ

The SEM can obtain grey-scale backscattered-electron (BSE) intensity images, which can be adjusted to visualise a specific range of electron densities using brightness and contrast settings. Each shade of grey represents an individual phase with a given chemical composition (mean atomic number) and forms a single crystal. Using ImageJ, captured BSE images can be analysed to provide a broad approximation of the average composition of a sample based on the classification of greyscale values. However, this approach comes with limitations. Minerals with similar average atomic numbers often produce overlapping greyscale values, making them difficult to distinguish, and complex mineral textures can increase the risk of misidentification. As such, ImageJ analysis should be regarded as only a broad approximation of modal mineralogy, rather than a precise quantification.

2.4 LA-ICP-MS

The analysis aimed to quantify REE concentrations in apatite, identify REE-bearing minerals and trace elements, and assess deleterious elements such as As, Th, and U. Samples were selected based on the results of SEM analysis, which determined their chemical composition. Laser ablation inductively coupled mass spectrometry (LA-ICP-MS) was performed at the Microgeochemistry Laboratory, Department of Earth Sciences, University of Gothenburg, using an ESI 213NWR laser apparatus coupled to an Agilent 8800 ICP-QQQ. Most samples were ablated using a 30 μm diameter laser beam, with the spot size occasionally reduced to

target-specific minerals. The laser-ablated material in the sample cell, which was transported by a helium stream (750 ml/min), was mixed downstream with N_2 (4 ml/min) and Ar (780 ml/min) and delivered to the ICP-MS. Reference materials included the NIST-SRM610 glass (Jochum et al., 2011), BCR-2G basaltic glass (Elburg et al., 2005), and Durango apatite (Lugo-Zazueta et al., 2024). Those were included in the measurement protocol every 15 analyses for quantification and monitoring instrumental drift throughout the working day (10/04/25).

2.4.1 Gathering data

Eight samples were selected: four from the iron ore (IO3, IO4, IO8, IO9), two from the hanging wall (HW7, HW11), and two from the footwall (FW1, FW2). All analyses were completed in a single day, yielding 216 data points, including 66 from standards. Most analyses focused on the iron ore samples, as they are compositionally diverse and represent Nordic Iron's primary mining target. The hanging wall samples showed similar compositions, requiring fewer analyses. Only two footwall samples were available, so both were included. A challenge during analysis was distinguishing visually similar minerals, such as xenotime from monazite and apatite from amphiboles, due to their comparable morphology in the microscope of the LA-ICP-MS. Despite this, enough analyses were performed to construct meaningful phase diagrams.

2.4.1 Data correction

The data was gathered in raw counts and then processed in GLITTER. Background subtraction was performed for each analysis. To convert the background-corrected counts into concentrations, internal standardisation was applied by assigning known or estimated concentrations of major elements for each mineral, based on values from Webmineral.com. Phosphorus (^{31}P) was used as an internal standard for apatite, monazite, xenotime, N610, and Durango, because of their consistently high phosphorus content. Silicon (^{29}Si) was used for BCR-2G and allanite, where silicon is a major constituent. Cerium (^{140}Ce) was used as the internal standard for uraninite, where neither P nor Si was suitable. Trace element concentrations were then calculated and normalised to CI chondrite values (McDonough & Sun, 1995). This step allowed the construction of preliminary REE patterns to detect potential errors. Once the chondrite-normalised data were considered reasonable, a correction was applied to account for variations in total oxide weight. Following the method of Liu et al. (2008), element concentrations were converted into oxide equivalents using molecular weights, summed, and then normalised to a total of 100 wt.%. This oxide normalisation was adjusted for differences introduced during internal standardisation and kept consistent between major and trace element datasets. Corrected values were then used for quantitative comparison and the following geochemical work. Arsenic concentrations measured by LA-ICP-MS were noticeably unreliable due to spectral interferences, likely originating from polyatomic species such as ^{35}Cl-$^{40}Ar^+$, which resulted in overlaps with the ^{75}As signal. A strong linear correlation was observed between measured As and the combined concentrations of Nd and Sm, suggesting that the apparent As signal was, at least in part, an artefact of interference associated with elevated REE contents. To correct this, an empirical adjustment was applied by subtracting a proportion of the As signal based on the Nd + Sm concentrations (Longerich et al., 1996). The correction significantly reduced the As concentrations in high Nd + Sm samples, with some values adjusted from 0.5 wt.% to below 500 ppm. Figure 7 is added, showing the original versus corrected As versus Nd+Sm concentrations, which indicate that there is not a significant overall change. Given that the overall change in total concentrations was less than 0.5 wt.%, renormalisation of the dataset was deemed unnecessary.

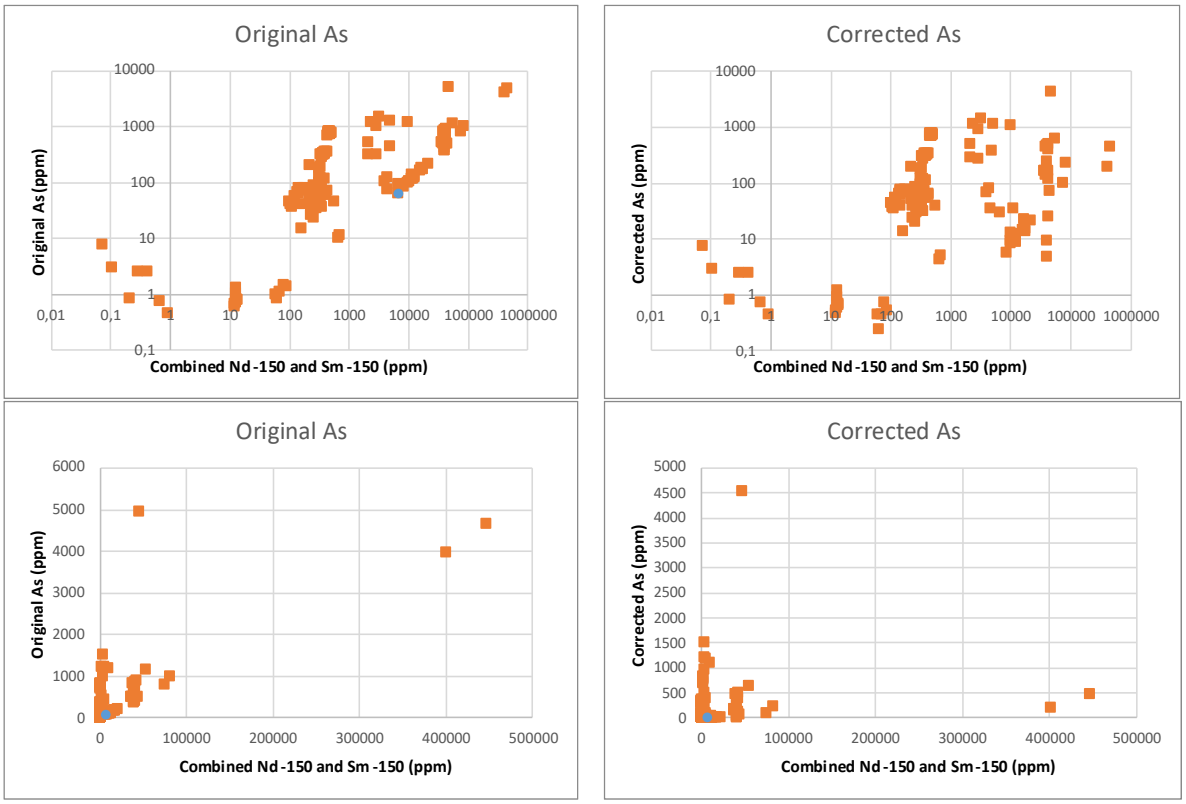

Figure 7: Scatter plots of original and corrected As concentrations (ppm) versus combined Nd-150 and Sm-150 concentrations (ppm), showing minimal overall change post-correction. The top plot covers a broader range (0.01 to 10000 ppm As) with a logarithmic scale, showing a dense cluster of high values. The bottom plot has a linear scale (0 to 6000 ppm As) with fewer data points, focusing on lower concentrations up to 6000 ppm.

3. Results

3.1 ALS data set

Using the geochemical data from ALS, intervals were divided into iron ore (Fe > 30%), host rock (Fe < 30%), and host rock directly adjacent to the ore. Chondrite-normalised REE patterns for these three groups are shown in Figure X. A t-test between ore and host rock gives means of 60.8 and 81.4 respectively, with p-values of 0.026 (one-tailed) and 0.052 (two-tailed), showing that the enrichment in the host rock is unlikely to be random. When splitting the host rock, the group adjacent to ore shows a mean of 77 compared to 67 in the more distal host rock, with p-values of 0.06 (one-tailed) and 0.12 (two-tailed). This indicates a weaker statistical signal, suggesting that enrichment near the ore is present but less pronounced, especially in the LREE, while MREE and HREE remain similar. Overall, the host rock is enriched in REE relative to ore, and this enrichment persists adjacent to the mineralization, but with a slightly different distribution that dampens the LREE while maintaining MREE–HREE levels.

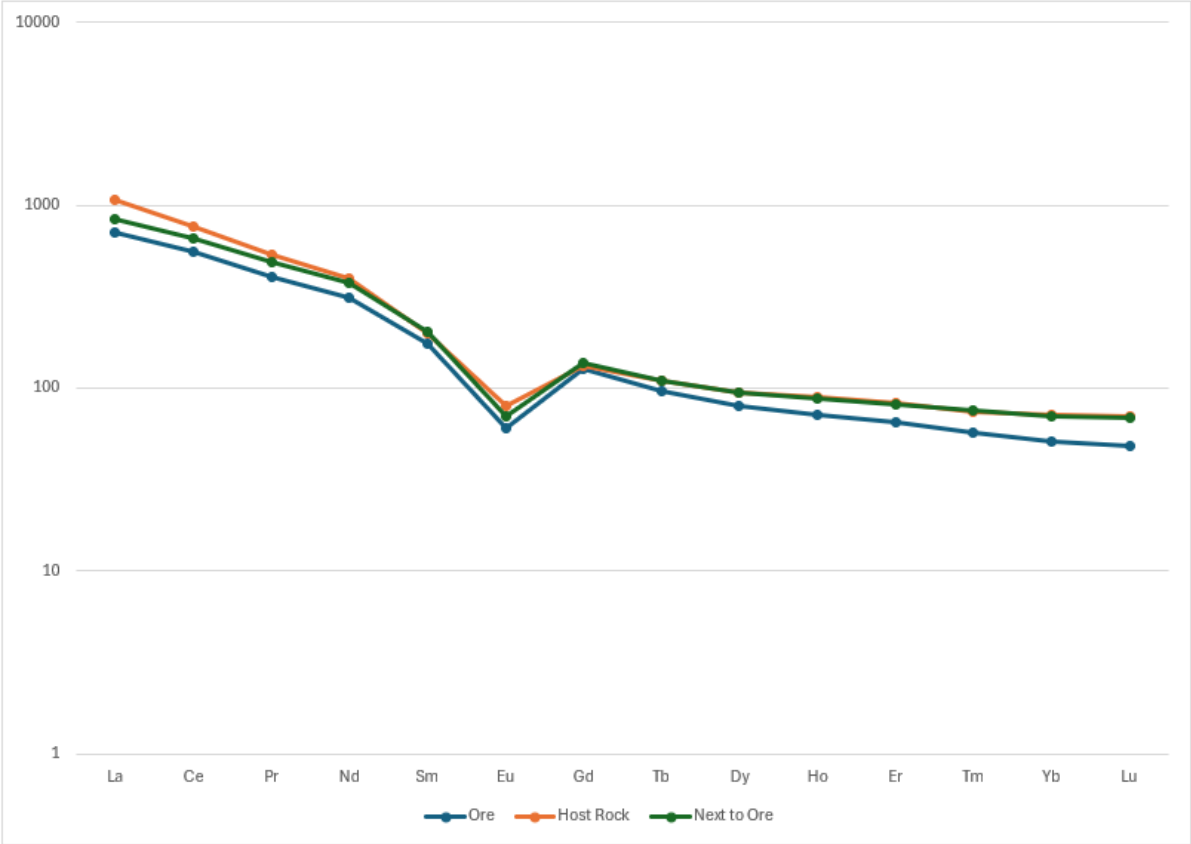

Figure 8: Chondrite-normalised REE patterns for ore, host rock, and host rock adjacent to ore. All groups exhibit similar overall trends, characterised by LREE enrichment, a negative Eu anomaly slightly less pronounced for the host rock, and flat MREE profiles, with slightly less HREE for the ore. Host rock is enriched relative to ore, while the adjacent host rock shows intermediate values with reduced LREE enrichment but similar MREE–HREE levels.

3.2 Minalyzer CS

Figure 9 and Figure 10 show Minalogger visualisations of the 50 kV XRF scans for the BB_14-008 drill core. Elemental data are overlaid directly on the core images, with the signal divided between cerium (Ce) and phosphorus (P) to enhance visual comparison. The first image displays a heatmap-style overlay, where warmer colours represent higher concentrations. A spatial correlation is observed between Ce and P in several core sections. The second image presents the same data using bar height and distinct colour coding to differentiate the elements, helping to find correlations between the two elements.

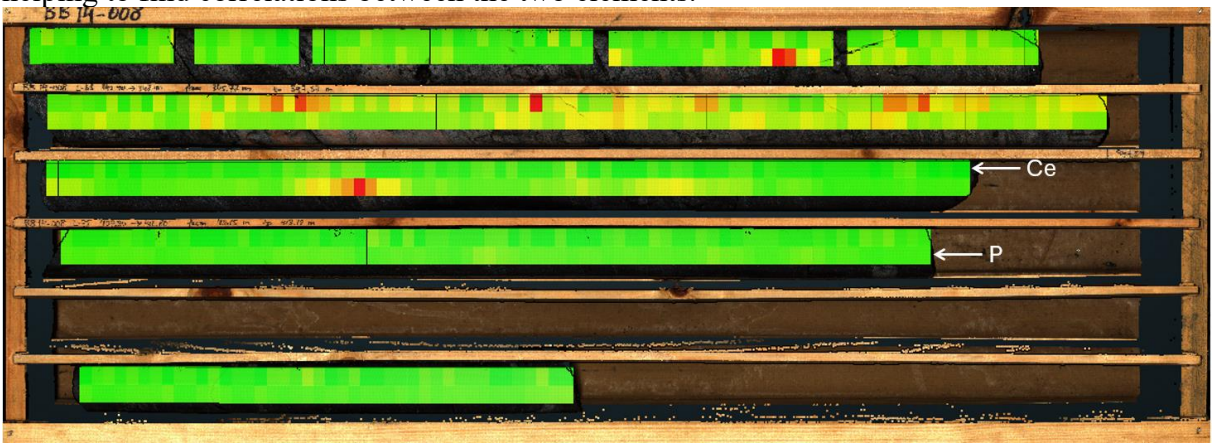

Figure 9. Cerium is represented in the top half, and Phosphorus in the bottom half. Minalogger raw spectrum visualisation.

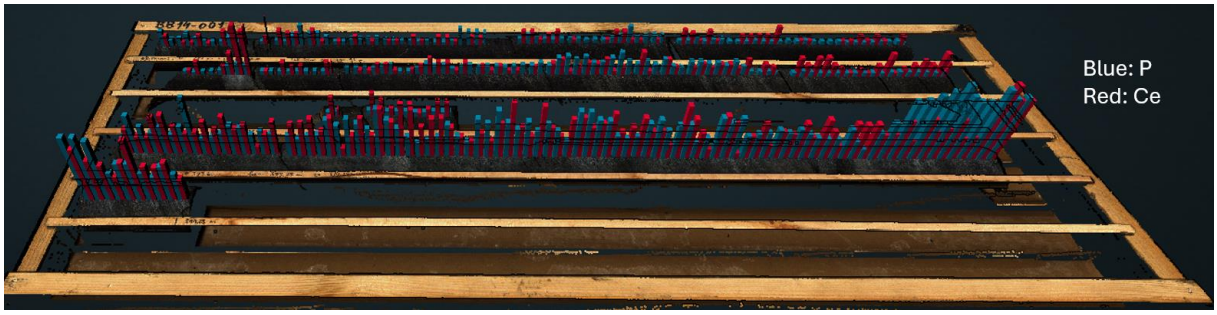

Figure 10. Same as for Figure 8, but with a different geochemistry visualisation style.

Eleven samples were created from the results of the Minalyzer CS. Table 4 highlights the values used in the sample selection. Figure 10 represents the location of the selected samples.

Sample	P	Ca	Ce	Y	Fe	Ti
FW1	2746	47748	19	4412	32612	446
FW2	2327	42569	27	4070	34726	326
HW5	785	7320	32	9971	149000	2402
HW6	1973	35654	9	626	157375	823
HW7	916	12884	34	9066	133552	1920
HW10	196	640	3	938	150735	4437
HW11	1116	16419	16	11407	133286	2887
IO3	398	3320	19	1237	22163	501
IO4	554	9508	4	354	321158	1194
IO8	164	935	7	645	136812	575
IO9	154	2140	5	330	258003	894

Table 4. Elemental concentrations (in ppm) for eleven selected samples based on Minalyzer CS results. Highlighted values indicate elevated concentrations of P, Ca, Ce, Y, Fe, or Ti, which were used as criteria in selecting samples for further LA-ICP-MS analysis. Sample locations are shown in Figure 9.

Figure 11. Sample number and locations. Pictures generated by the Minalyzer CS.

3.3 SEM analysis

Phases that were deemed important for this study are listed in Table 5.

Sample	Borehole	Description	Fap	Mnz	Xtm	Mag	Hem	Ilm	Bsn	Aln	Zrc	Ura
FW1	BB14-001	fine laminated dark/white banding	+	+	+	+	+		+	+		
FW2	BB14-001	fine dark/white slight lamination, REE-rich	+	+	+	+	+		+	+	+	
IO3	BB14-001	white alteration zone, iron ore	+	+	+	+		+			+	+
IO4	BB14-001	fine dark/white laminated banding	+	+		+		+		+		
IO8	BB14-008	red inclusion, alteration zone, REE-rich	+	+			+				+	
IO9	BB14-008	red inclusion, alteration zone	+	+	+	+	+			+	+	
HW5	BB14-008	large crystalline vein	+	+	+	+	+				+	
HW6	BB14-001	massive, dark, fine-grained, iron ore	+	+	+	+	+				+	+
HW7	BB14-008	white alteration zone, iron ore	+	+		+	+	+	+	+	+	
HW10	BB14-008	red inclusion, alteration zone, Ti rich		+	+	+	+				+	
HW11	BB14-008	red inclusion, alteration zone	+	+	+	+	+				+	

Table 5. Presence or absence of mineral phases in samples. No quantification performed; the presence of a single grain is marked as "+". FW = Footwall, HW = Hanging Wall, IO = Iron Ore. Fap = Fluorapatite, Mnz = Monazite, Xtm = Xenotime, Mag = Magnetite, Hem = Hematite, Ilm = Ilmenite, Bsn = Bastnäsite, Aln = Allanite, Zrc = Zircon, Ura = Uraninite.

3.3.1 Footwall

Sample FW1 and FW2

Two samples of the footwall were analysed. Figure 12 shows selected features found in the BSE. The composition is nearly identical for the two samples. The groundmass is primarily composed of fluorapatite, biotite, quartz, orthoclase (K-feldspar), and actinolite (Ca-amphibole), with the presence of both magnetite and hematite. The majority of the fluorapatite grains are euhedral or subrounded and form aggregates with quartz, which occurs as crack-filling. Subordinate phases such as titanite and REE-bearing minerals, allanite-(Ce), xenotime-(Y), and monazite-(Ce) can be found. However, allanite constitutes the most significant proportion of the sample secondary minerals and is the most abundant REE mineral. The grains, ranging from 10 to 500 µm in diameter, exhibit distinct angular or anhedral forms, especially when filling existing spaces, such as cracks, voids, or grain boundaries, often within or adjacent to fluorapatite and the silicate groundmass. They frequently occur as aggregates or inclusions within larger fluorapatite crystals and are commonly found as crack-fillings in veins. Allanite displays irregular or interstitial shapes, conforming to available space. Small inclusions are frequently scattered within larger fluorapatite crystals, and most are found acting as crack fillings in veins. Some allanite crystals contain BSE-bright zoning, indicating an enrichment in heavier elements, specifically a higher concentration of Ce, La (± Nd). Monazite and xenotime can also be found occurring along grain boundaries, but compared to allanite, they appear in subordinate amounts. The grain sizes are around 30-50 µm for the monazite and around 10-30 µm for the xenotime. Bastnäsite and fluocerite were also found to occur along cracks and as veins, forming linear concentrations that follow the fractures in the fluorapatite, as well as disseminated within fluorapatite grains. Titanite grains are present in lower amounts, with crystals reaching up to 300 µm in size and exhibiting different shades, indicating enrichment in yttrium, a common substitution in titanite.

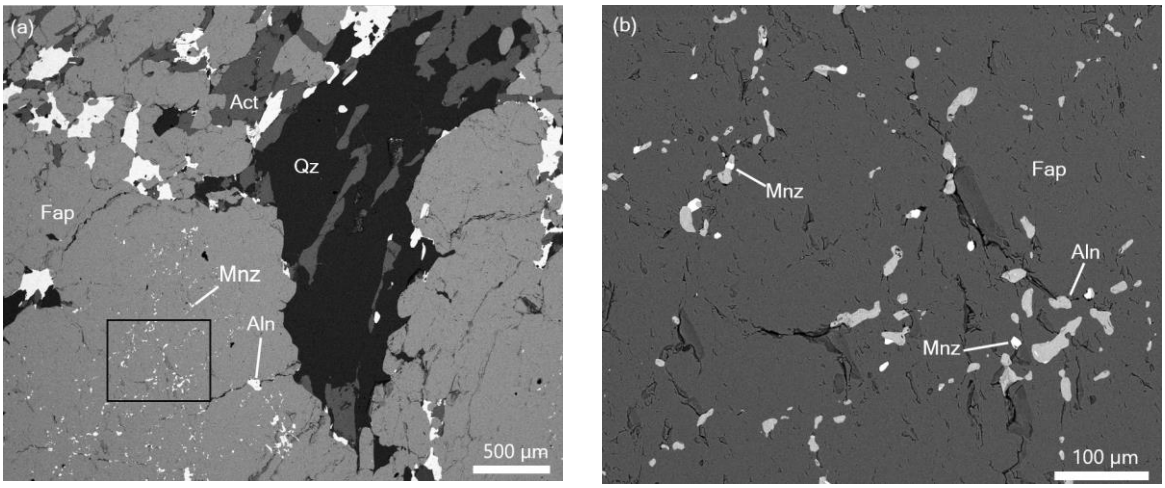

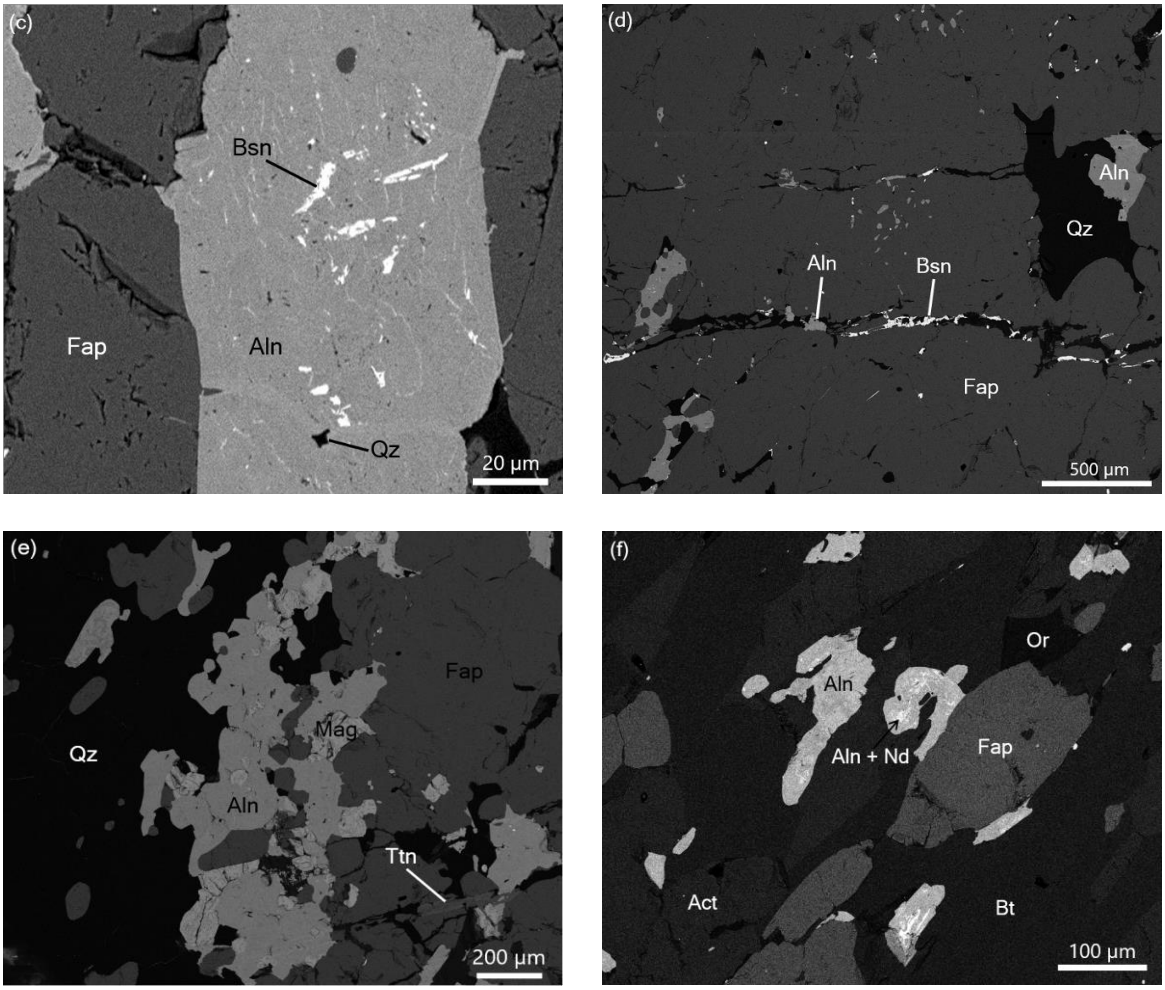

Figure 12. High-contrast BSE images of texture in the footwall samples in the Blötberget magnetite-hematite-apatite ores. (a) Disseminated inclusion grains of allanite and monazite in fluorapatite. (b) Enlargement of the box in (a). (c) Allanite grain containing bastnäsite. (d) Vein of quartz containing bastnäsite going through apatite. (e) Large allanite grain enclosing magnetite between apatite and quartz. (f) Nd enriched allanite grains in a groundmass of biotite, anorthoclase, and apatite.

3.3.2 Hanging wall

The hanging wall composition is similar with slight variations for all samples. Figure 13 displays maps of the various samples, and Figure 13 highlights several notable features. Quartz, orthoclase, biotite, fluorapatite, and hematite-magnetite are the main components of it. Subordinate phases are also present, such as amphibole (a solid solution of cummingtonite and grunerite) and phlogopite, muscovite, and chlorite. Monazite and xenotime are the two most common REE minerals that can be found in the hanging wall. A single occurrence of allanite was found in one of the five samples, and no vein-forming REE minerals, such as bastnäsite or fluocerite, were identified.

Sample HW5, HW7, HW11

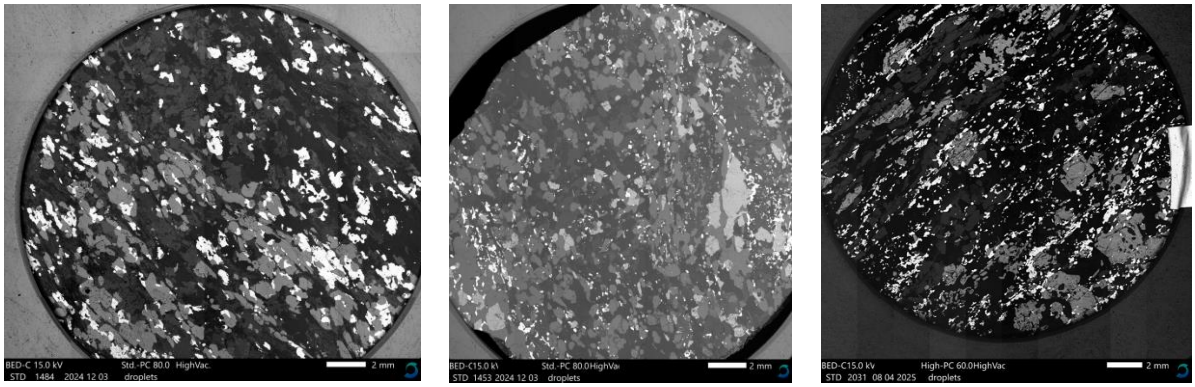

Figure 13. Samples HW5, HW7, and HW11 exhibit a clear flow orientation. In HW5 and HW11, all crystals are strongly oriented, whereas in HW7, primarily monazite and xenotime grains display a slight orientation.

Ce and Ti contents from the Minalyzer CS in these three samples were above average, with an extremely high amount of Y. The amount of REE minerals varies greatly between different parts of the hanging wall. In these three cases, the contents of monazite and xenotime were extremely high. The amount and size of REE minerals appear to be correlated. Xenotime and monazite grains are typically rounded and appear to crystallise in contact with, adjacent to, or directly as inclusions within iron oxides or apatite. In contrast, apatite crystals are euhedral and commonly occur as aggregates. Monazite grains are equigranular, rounded, and range from 20 µm up to 630 µm, with an average of ~100 µm. Xenotime grains are smaller, ranging from 10 µm to 140 µm, with an average size of ~50 µm; however, they have a similar shape to monazite, making them more challenging to differentiate. The identified xenotime grains were consistently located around iron oxides and feldspars.

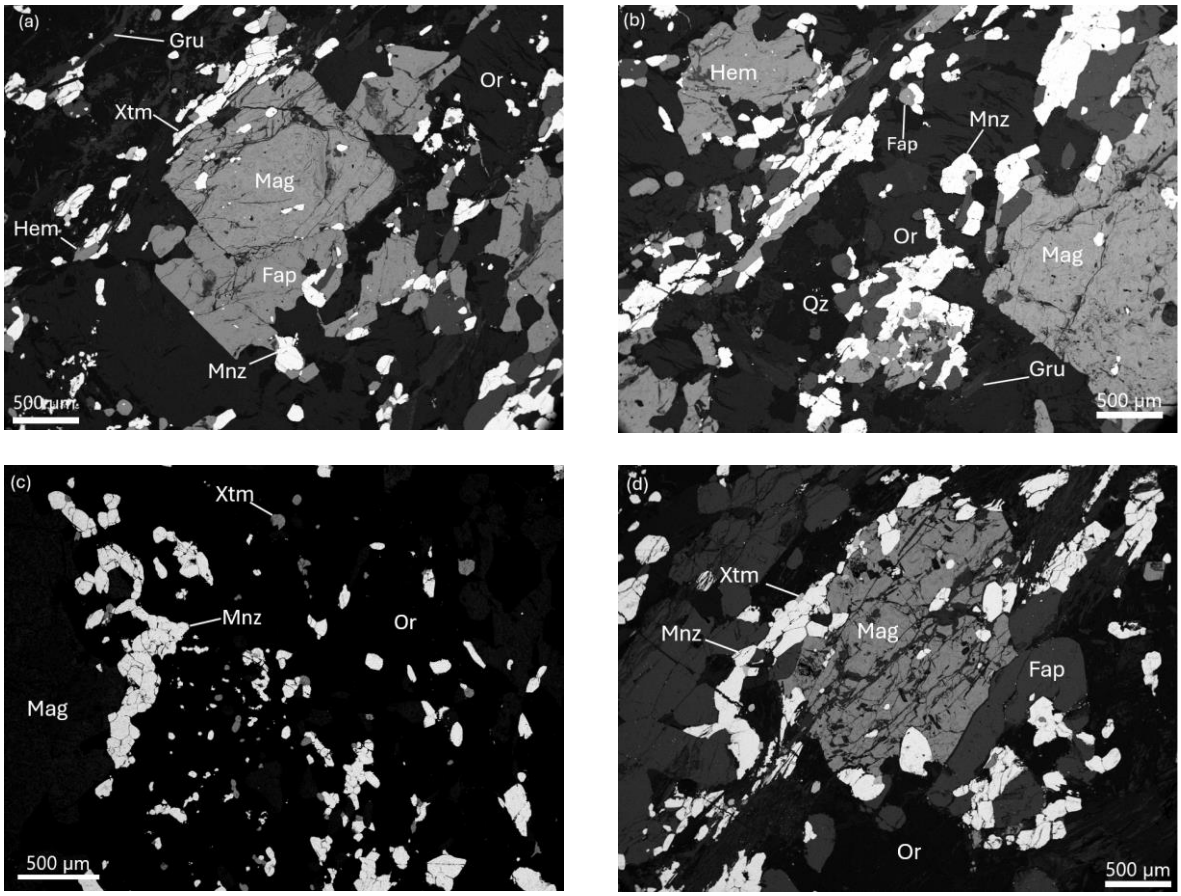

Figure 14. (a) Magnetite overgrowing an apatite grain in a groundmass of anorthoclase with monazite and xenotime inclusions. (b) Hematite containing inclusions of monazite and magnetite separated by apatite and monazite. (c) A 2mm-wide chain of monazite adjacent to a 4x2mm magnetite with xenotime. (d) Significantly altered magnetite with large inclusions of monazite and xenotime surrounded by apatite, which hosts small monazite grains in grain boundaries and inside it.

Sample HW6

This sample showed the highest apatite content, which aligns with Minalyzer CS data, and contained a low amount of iron oxides. It is the only sample with an allanite grain and includes small and rare xenotime and monazite crystals.

Sample HW10

Sample HW10 is characterised by high Ti and low Ca and P, as indicated by the absence of apatite. The elevated Ti concentration is explained by the higher abundance of Ti-bearing hematite in the sample.

3.3.3 Other features in the hanging wall

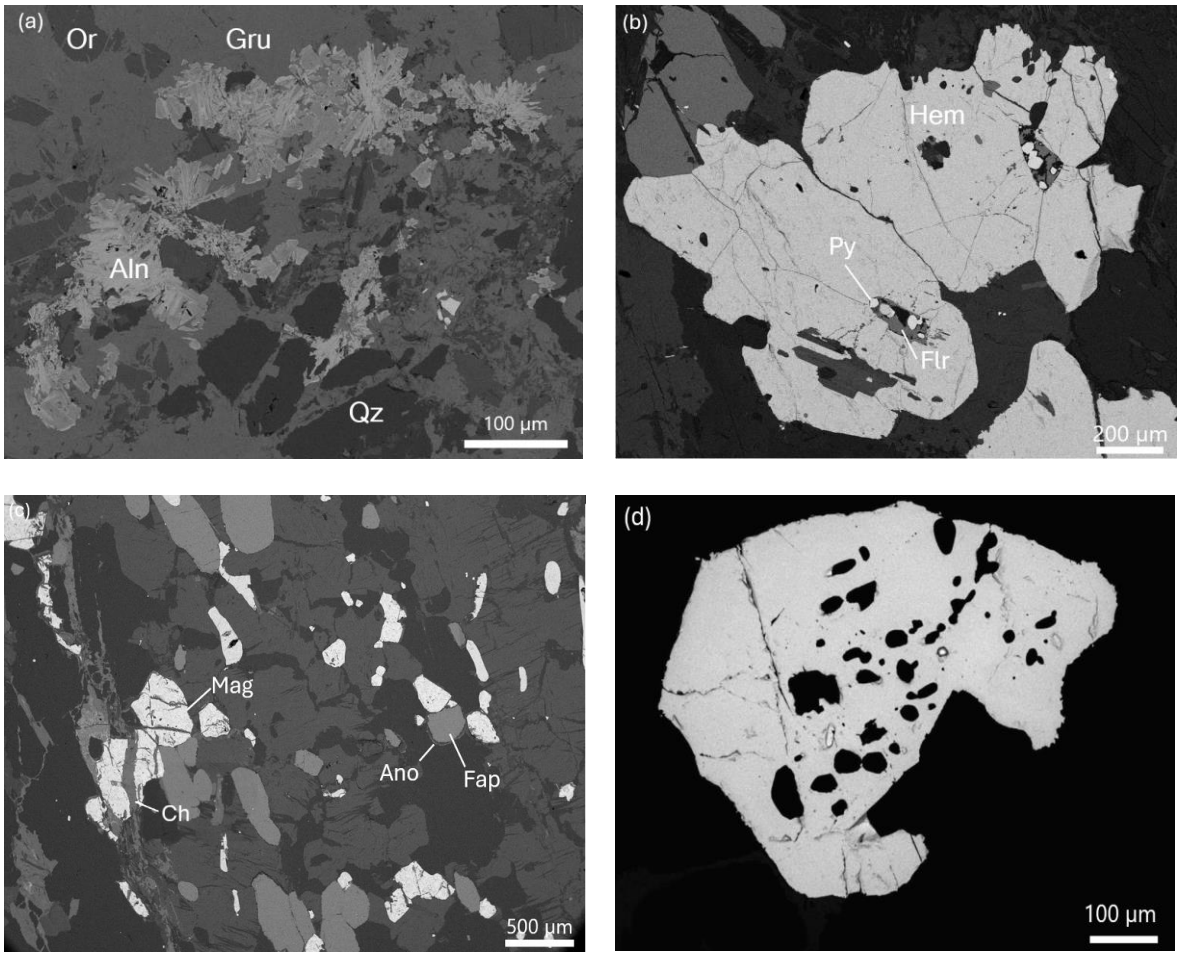

Figure 15. (a) Altered grain of allanite from HW6. (b) grain of hematite with fluorite inclusions containing pyrite. (c) Magnetite crosscut by chlorite and fluorapatite, being altered by anorthoclase. (d) Most prominent grain of monazite in all samples, 630µm.

3.3.4 Iron Ore

Figure 16 displays different interesting parts of the iron ore samples.

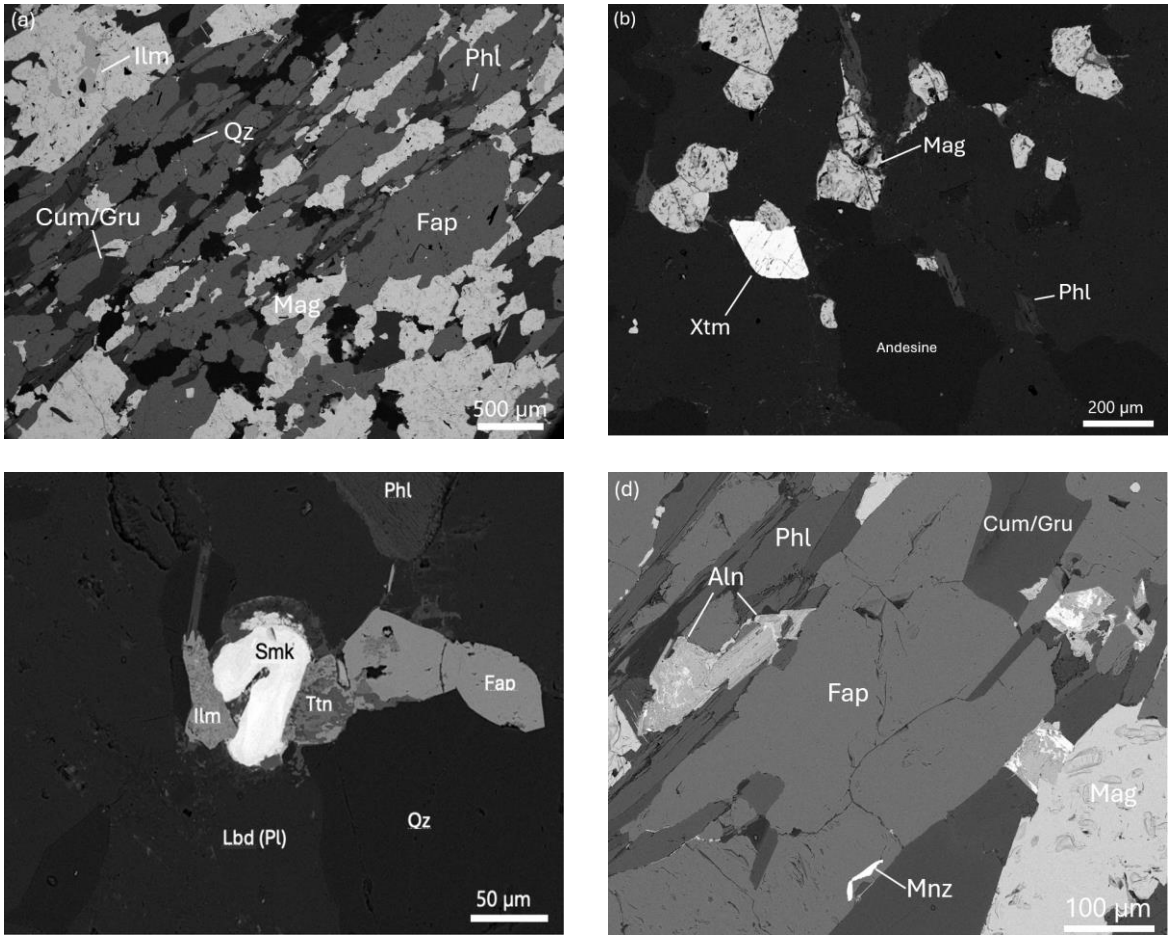

Figure 16. (a) A vein containing diverse minerals crosscuts the magnetite. (b) Unaltered xenotime and magnetite grains. (c) IO3 Samarskite surrounded by various minerals. (d) Fluorapatite grain with allanite, where whiter areas are enriched in Ce and La.

Sample IO8

IO8 has the lowest concentrations of elements like Ca, Y, and P compared to other samples. It is composed of a groundmass of actinolite, biotite, albite, and iron oxides, with minor apatite grains. However, xenotime, monazite, and zircon are easily found, often accompanied by small thorite crystals. Monazite and xenotime grains occur within heavily altered iron oxides.

Samples IO3

IO3 exhibits a lower iron content compared to the average of other samples. It has a groundmass rich in phlogopite, quartz, and cummingtonite, with magnetite as the only iron oxide. For REE minerals, monazite dominates, with sizes ranging from 20 to 200 µm and a slight enrichment in Nd in some zoned grains. Xenotime grains are rare but, when found, are large (up to 250 µm) and have a dipyramidal shape. Sample IO3 is the only one with rounded magnetite. Few zircons are present, ranging from 10 to 40 µm. Uranium-bearing minerals, including thorite and uraninite, occur as small grains, typically around 10 µm, with a few instances of grains exceeding 50 µm in size. Three samarskite crystals, a REO mineral ($(Y,Fe^{3+},Fe^{2+},U,Th,Ca)_2(Nb,Ta)_2O_8$) containing niobium, tantalum, yttrium, and minor radioactive elements, were identified in the sample alongside a complex variety of minerals, such as ilmenite, titanite, labradorite, and a solid solution of fayalite and forsterite.

Sample IO4 and IO9

IO4 and IO9 are similar. Both possess high calcium levels, as shown by Minalogger, due to their abundance of allanite and titanite. They consist of a groundmass of phlogopite, quartz, cummingtonite, and grunerite. A notable difference is that IO4 lacks hematite, while IO9 contains both hematite and magnetite. IO9 has more allanite than monazite or xenotime, with allanite grains always zoned with higher Ce and La content. For both samples, allanite grains range from 30 to 250 μm; no uranium minerals are present. Nearly all REE minerals are found next to or within magnetite and apatite.

ImageJ

Using ImageJ gave an approximation of mineral proportions, highlighting significant variations in apatite, iron, and gangue content across the samples, while also showing notable REE enrichment in specific instances such as IO9 and HW11.

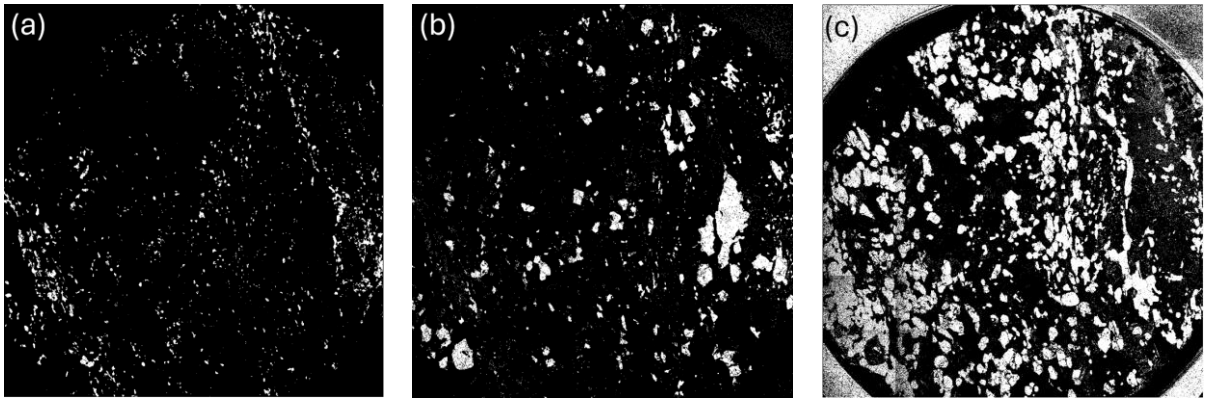

Figure 17. Images representing each one as an individual phase in white: (a) monazite + xenotime, (b) iron oxide, (c) apatite abundance in sample HW7.

	Apatite (%)	**Iron (%)**	**Gangue (%)**	**REE (%)**
FW1	50.36	6.25	42.92	Aln: 0.47
FW2	50.56	15.48	29.97	Aln: 3.99
IO3	3.61	9.33	86.06	REE: 1
IO4	13.61	40.49	45.87	n/a
IO8	n/a	55,21	44,79	n/a
IO9	3.01	58.92	29.03	Aln+Ilm: 9.02
HW5	19.02	8.30	70.33	Mnz: 2.35
HW6	54.46	5.62	39.99	n/a
HW7	34.90	8.18	53.44	Mnz + Xtm: 3.49
HW10	7.77	n/a	92.23	n/a
HW11	12.79	16.28	62.79	Mnz + Xtm: 8.14

Table 6. FW1 and FW2 values. “Gangue” is the non-economic minerals in a sample. All values are expressed and normalised to 100%. “n/a” means that the values were too low to be measured.

3.4 LA-ICP-MS

3.4.1 Apatite

The collected data is organised into tables and diagrams. Apatite compositions are generally consistent across samples, with notable enrichment in the hanging wall, while the footwall and iron ore show similar, less enriched values. Values for the major elements in the apatite are presented in Table 7, and the values for trace elements are listed in Table 8. Those values are chondrite-normalised and depicted in Figures 18, 19, and 20.

	FW1	FW2	HW7	HW11	IO4	IO9
TREO	0,25	0,18	0,28	0,29	0,18	0,20
P_2O_5	40,78	39,39	39,27	39,87	40,61	40,29
F^-	8,02	8,70	8,29	9,05	8,85	8,00
MnO_2	0,03	0,02	0,06	0,06	0,02	0,03
Na_2O	0,06	0,04	0,11	0,11	0,04	0,04
MgO	0,01	0,01	0,04	0,03	0,06	0,03
SiO	0,11	0,09	0,08	0,08	0,15	0,17
Cl^-	0,05	0,05	0,05	0,04	0,05	0,06
CaO	51,02	51,70	52,10	50,76	50,22	51,38

Table 7. Averages of wt.% for major elements in apatite of different samples. F^- is not measured accurately by the SEM.

	FW1	FW2	IO4	HW7	IO9
La	84,96	65,62	204,47	112,35	40,78
Ce	454,45	267,96	711,84	460,11	177,75
Pr	103,26	55,57	119,25	86,94	38,60
Nd	702,06	373,94	622,79	531,41	297,42
Sm	259,56	163,33	201,18	175,39	148,52
Eu	26,45	19,49	51,93	20,13	19,49
Gd	334,39	243,86	279,25	230,01	254,97
Tb	48,90	36,47	54,66	32,58	40,66
Dy	301,62	223,37	393,20	203,16	264,51
Ho	60,21	45,18	80,01	41,01	55,16
Er	163,99	121,98	210,05	112,10	153,21
Tm	19,96	14,42	23,89	13,32	18,56
Yb	111,07	79,42	121,88	73,68	104,83
Lu	13,91	10,24	13,62	9,68	13,78
Y	1808,07	1371,91	2150,81	1277,28	1659,48

Table 8. Averages of REE in ppm for all measured apatite in different samples.

The distribution of Total Rare Earth Oxides (TRE_2O_3) per analysed groups of apatites is listed in Table 9. The TRE_2O_3 value was calculated by summing the oxides of all lanthanides (La to Lu), using the following formula:

$$La_2O_3\ (wt\%) = \left(\frac{La\ (ppm) \times \text{Atomic mass of La} \times 2}{\text{Molecular weight of } La_2O_3}\right) \div 10,000$$

The total TRE_2O_3 (wt%) was then obtained by summing:

$$TRE_2O_3 = \sum(\text{REE concentration} \times \text{Atomic mass} \times 2/\text{Oxide mass}) \div 10,000$$

This includes La, Ce, Pr, Nd, Sm, Eu, Gd, Tb, Dy, Ho, Er, Tm, Yb, and Lu.

Location	Average LREE (wt.%)	Average HREE (wt.%)	Average TREE (wt.%)
Footwall	0,130	0,098	0,228
Hanging wall	0,132	0,094	0,226
Iron ore	0,129	0,091	0,220

Table 9. Concentrations of LREEs, HREEs, and TREEs in the apatites for this study (wt.%).

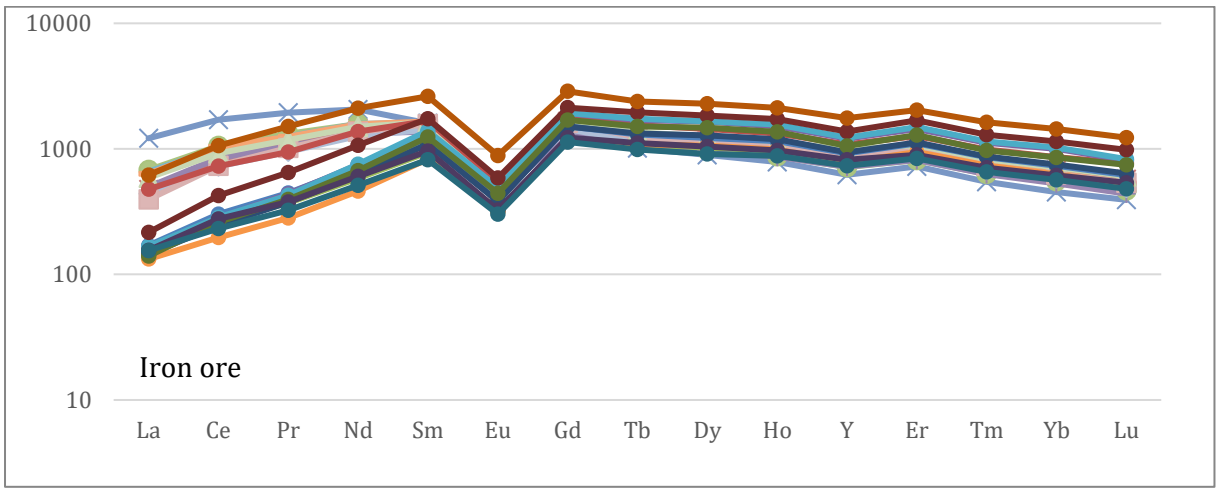

Figure 18. Chondrite normalised representation of the REE concentration for the apatite in the iron ore samples.

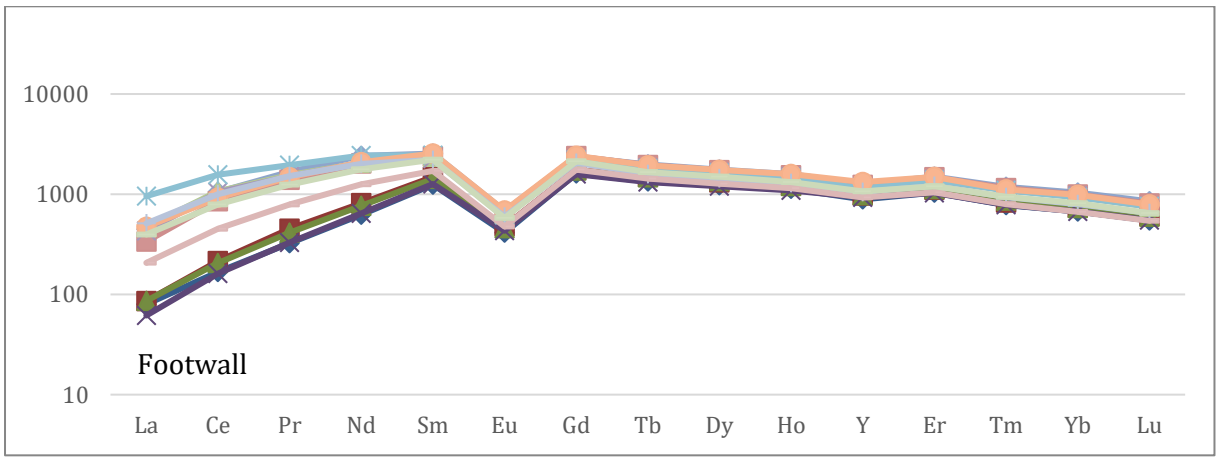

Figure 19. Chondrite normalised representation of the REE concentration for the apatite in the footwall samples.

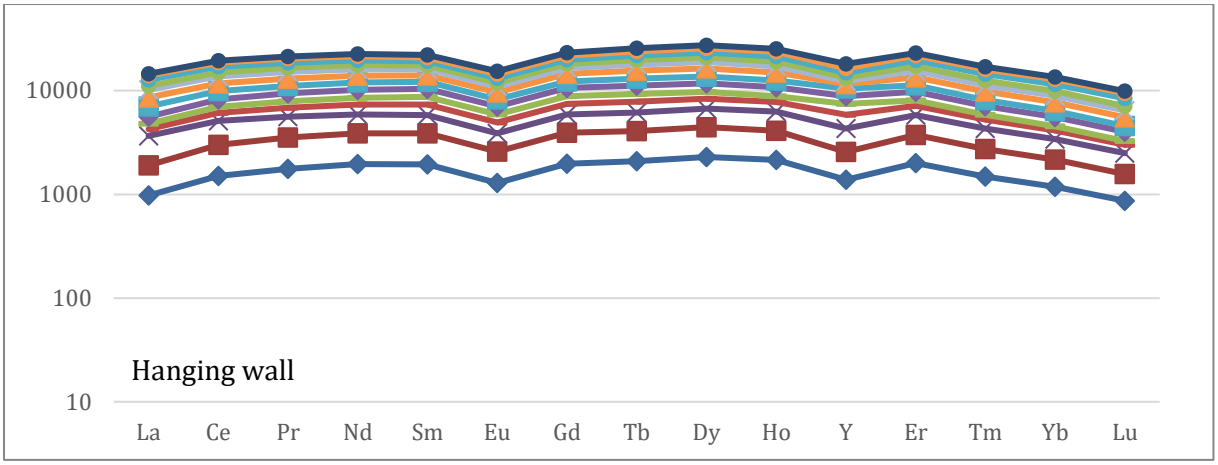

Figure 20. Chondrite normalised representation of the REE concentration for the apatite in hanging wall samples.

3.4.2 Monazite, xenotime, allanite, and other phases

Phosphorus was used as an internal standard for phases such as monazite and xenotime; thus, their concentration was fixed to a theoretical stoichiometric value. The full amounts are listed in the appendix. Tables 9 and 10 display the values for monazite and xenotime, respectively, while Table 11 presents the values for allanite.

	HW	IO	FW
P	130926	130926	130926
Ca	2993	1290	489795
V	54	83	487
Ga	5912	6461	3095
As	610	407	487
Y	12061	3592	5785
La	211957	209179	79237
Ce	322554	352210	210120
Pr	30485	32434	28225
Nd	102266	109211	113254
Sm	12182	9918	13875
Eu	2061	522	828
Gd	7985	4753	6319
Tb	904	340	521
Dy	4267	1228	1864
Ho	574	157	237
Er	995	275	455
Tm	75	21	48
Yb	265	77	256
Lu	21	7	31

Table 9. Averages of ppm for major and minor elements constituting monazite in different samples (HW n=8, FW n=2, IO n=3). The phosphorus value is theoretical.

3.4.3 Xenotime

	IO3	HW7
Si	5665	1361

P	170204	170204
Ca	5093	13599
As	103	1048
Y	422524	446883
La	275	6684
Ce	1222	12453
Pr	393	1405
Nd	4118	6299
Sm	5759	4209
Eu	677	1855
Gd	19338	15929
Tb	5402	4932
Dy	51590	53078
Ho	13667	14832
Er	48040	51643
Tm	7903	7619
Yb	60224	50134
Lu	8239	6319
Th	7739	97
U	16523	248

Table 10. Averages ppm for major and minor elements constituting xenotime in different samples (IO n=3, HW n=8). The complete amounts are listed in the appendix. The phosphorus value is theoretical.

3.4.4 Allanite

Mg	15555	6448
Al	90306	81525
Si	153086	146344
Ca	74155	76996
Fe	97225	90774
As	125	128
Y	3248	2242
La	36516	44159
Ce	69241	87463
Pr	7667	9328
Nd	30399	32394
Sm	4860	3527
Eu	448	216
Gd	2935	1736
Tb	270	149
Dy	1043	608
Ho	133	89
Er	250	212
Tm	24	27
Yb	123	184

Lu	15	25
Th	1146	1565
U	193	121

Table 11. Average ppm for major and minor elements constituting allanite in different samples (IO n=4, FW n=13). The complete amounts are listed in the appendix.

3.4.5 Arsenic, Uranium, Thorium

The deleterious elements observed in the samples were collected along with the other elements and are displayed in Table 12. A comparison with other studies is done in the discussion.

Mineral	Sample	**As**	**Th**	**U**
Apatite	FW	47	0,81	2,89
	HW	96	0,47	2,19
	IO	87	0,42	3,60
Xenotime	IO	147	7739	16523
	HW	988	97	248
Monazite	FW	66	336	253
	HW	223	1056	92
	IO	250	18895	129
Samarskite	IO	17	36095	47302
Allanite	IO	258	1146	193
	FW	1210	1453	113
Bastnäsite	FW	125	1	12

Table 12. Average in ppm of As, Th, and U in apatite and REE-bearing minerals from the Blötberget deposit.

4. Discussion

4.1 SEM

4.1.1 ALS Data

When comparing enrichment in the different parts of the drill cores, it is evident that the adjacent host rock remains enriched compared to the ore, but its REE pattern differs less strongly from that of the distal host rock. This may reflect interaction at the ore–host contact, like partial redistribution, while the broader enrichment of MREE–HREE is a more systematic feature of the host lithology.

4.1.2 Iron oxides in the hanging wall

The two iron oxides, hematite and magnetite, are challenging to differentiate in the SEM due to their similar chemical compositions; however, they can be distinguished by their texture and elemental content. In the studied iron oxides of the hanging wall, it was discovered that hematite contains 4–11% titanium, incorporated through substitution in its structure since it forms a solid solution with ilmenite ($FeTiO_3$). Magnetite has a more complex surface texture. The grains appear irregular, exhibiting angular and sharp edges. The magnetite also exhibits irregular protrusions on its surface, a common feature during formation or alteration, resulting in a rougher appearance. The grains exhibit a high degree of fracturing, with visible cracks and fissures extending throughout the mineral. Magnetite exhibits greater alteration than hematite

due to its cubic spinel structure, which is more brittle and susceptible to weathering-induced microfractures. In contrast, hematite's trigonal structure increases its resistance to alteration (Nesse, 2023). Hematite's smoother, less angular appearance under SEM aligns with its characteristic platy or tabular crystalline habit, which often appears more polished and uniform compared to magnetite.

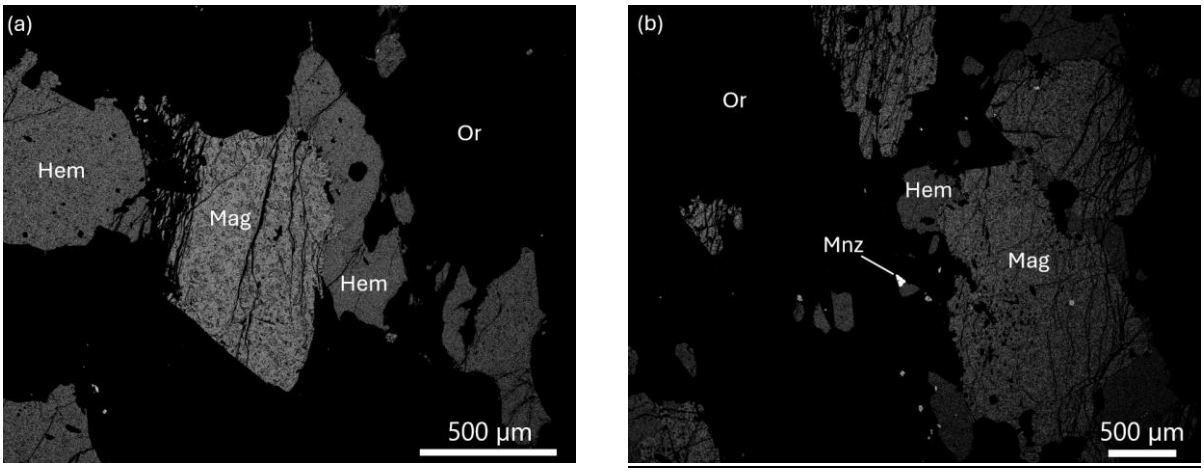

Figure 21. Hematite and magnetite of HW10 in a groundmass of orthoclase.

4.1.3 Apatite

The Ca, P, and F contents in the apatites of this study (Blötberget) are comparable to those of Kiruna-type apatites as seen in Table 13 (Lindbom, 2016; Mao et al., 2016).

	CaO	P_2O_5	F
Blötberget	54,11	42,51	3.38
Kiruna-type	54.71	40.97	3.69
Per Geijer	54.60	42.45	3.57

Table 13. Average values with n = 43 in the apatite concentration of different IOAs.

4.1.4 REE phases formation

Allanite is the dominant REE phase in the footwall, whereas monazite and xenotime dominate in the hanging wall and iron ore zones. The experimental work by Harlov (Harlov et al., 2005; Harlov & Förster, 2004) significantly advanced the understanding of how monazite and xenotime form as tiny inclusions within fluorapatite or at its edges in various samples. This research provided detailed insights into the fluid-induced coupled dissolution-reprecipitation mechanism, a process also observed by Jonsson et al. (2016) in Grängesberg. The authors suggest that REE-rich apatite formed first, then broke down due to fluid activity, leading to the formation of monazite and xenotime. In some samples, these monazite grains grew larger through Ostwald ripening. This mechanism explains how REE-bearing phosphate minerals can form directly when fluorapatite breaks down. It was discovered through experiments that, as hot, watery fluids move through fluorapatite, they create microscopic pores (micro- and nano-porosities). These pores allow fluids to penetrate the apatite and transport elements, effectively reconcentrating REEs already present in the apatite into new, distinct mineral grains rather than introducing new external sources of elements. Later experiments further confirmed that Ostwald ripening is the primary process causing these newly formed inclusions to grow larger, a mechanism experimentally observed at temperatures ranging from 300 to 900°C. This occurs as smaller crystals dissolve and their material is added to larger ones, resulting in fewer but larger grains. This mechanism is observed throughout the study areas and would explain why

many larger monazite and xenotime grains are found adjacent to fluorapatite. In the samples of this study, the larger grains grew larger due to fluid pathways, as visible in Figure 11, created by the dissolution-reprecipitation process, which facilitated efficient element transport. This enabled components from dissolving small inclusions to contribute to the growth of larger grains, which might be at the edges of the apatite or in nearby fluid-rich domains. This process is a significant factor in the growth of monazite and xenotime in the Blötberget deposit. In this study, it is demonstrated that REEs, initially held within a host mineral such as apatite, are internally remobilised and recrystallised due to hydrothermal alteration in the Blötberget IOA, similarly to their peers. The primary source of these REEs is apatite dissolution, which occurs during late to post-magmatic stages when hot, chemically active hydrothermal fluids carrying elements such as chlorine from hydrochloric acid and sulfur from sulfuric acid, derived from both magmatic volatiles and mobilised formation waters, permeate the ore body. Areas with high concentrations of monazite and xenotime in this study clearly show apatite's capacity as a substantial REE reservoir (Harlov et al., 2002, 2005; Harlov & Förster, 2004; Jonsson et al., 2016).
The influence of dissolution–reprecipitation processes, essential to a late-to post-magmatic hydrothermal system, is reflected in the oriented arrangement of monazite, xenotime, apatite, and iron oxides observed in both the hanging wall and footwall, as well as in some iron ores. While this alignment likely developed in response to circulating hydrothermal fluids, it may also record one or more phases of deformation associated with the Svecokarelian orogeny, which imposed changing stress fields capable of reorienting or recrystallising these minerals in the rocks. The absence of a similar alignment in the surrounding groundmass suggests either that deformation and fluid flow were focused in REE- and apatite-bearing zones, or that the matrix minerals were less sensitive to reorientation under the prevailing conditions. Although the Svecokarelian orogeny provides a plausible regional tectonic framework, attributing the observed mineral alignment directly to this event remains speculative in the absence of detailed structural analysis. The textures are therefore best interpreted as the combined result of late-to post-magmatic hydrothermal processes, potentially modified by regional deformation.

Jonsson et al. (2016) noted that allanite typically occurs adjacent to fluorapatite with minimal monazite/xenotime inclusions. This study could expand the understanding of REE mineral formation to include other REE-bearing minerals. Allanite is a Ca-REE silicate mineral, so its formation requires calcium and REE enrichment in a silicate system. The elevated Ca concentrations in the Minalyzer CS data are consistent with conditions favourable for allanite formation. Allanite was observed forming as fracture-filling and in the groundmass, suggesting precipitation from a REE-bearing fluid, potentially during late-stage alteration rather than solely early metamorphism. Observations from the footwall (e.g., Images a–c of Figure 11) show that allanite also occurs as inclusions within apatite, exhibiting textures and grain sizes consistent with Ostwald ripening, as described in previous studies for monazite. This suggests that allanite may undergo coarsening processes both as inclusions and adjacent grains, unlike the mechanism proposed by Jonsson et al. (2016), which had only linked allanite growth to the reactions with the surrounding silicate matrix. The co-occurrence of allanite and monazite within single apatite grains indicates a closer genetic relationship between these phases in specific settings (Jonsson et al., 2016).
Figure 14(a) shows a highly altered allanite alongside chloritized coronas. Previous work on REE minerals in pelitic rocks has shown that near the chloritoid-out zone, allanite and its rims are partially to fully replaced by xenotime and monazite. Those replacements are associated with quartz and biotite, which are heavily present in the hanging wall. Although no trace of monazite forming as rims could be found, the known presence of monazite (±xenotime) in the hanging wall could reflect the breakdown of allanite in a low calcium, high temperature

environment (Janots et al., 2007, 2008, 2011). This is a possibility, but there is no direct evidence to support it. More samples could be needed to make this observation. The reverse scenario, allanite from monazite, is also experimentally supported, consistent with experimental data (Budzyń et al., 2017). In the footwall, discrete bastnäsite grains disseminated within allanite and larger grains along veins suggest that Ostwald ripening or fluid-mediated growth also influenced bastnäsite formation. This aligns with (Majka et al., 2022), which described REE-fluorocarbonates coronas forming around monazite due to CO_2-rich fluids. These findings underline the role of fluid pathways in promoting dissolution-reprecipitation and Ostwald ripening, not only for monazite and xenotime in fluorapatite but also for allanite and bastnäsite in their respective hosts.

4.2 LA-ICP-MS

4.2.1 Apatite

The REE profile of the two drill cores used in this study reveals that the footwall drill hole exhibits a strong negative Eu anomaly compared to the hanging wall, which is significantly less pronounced.

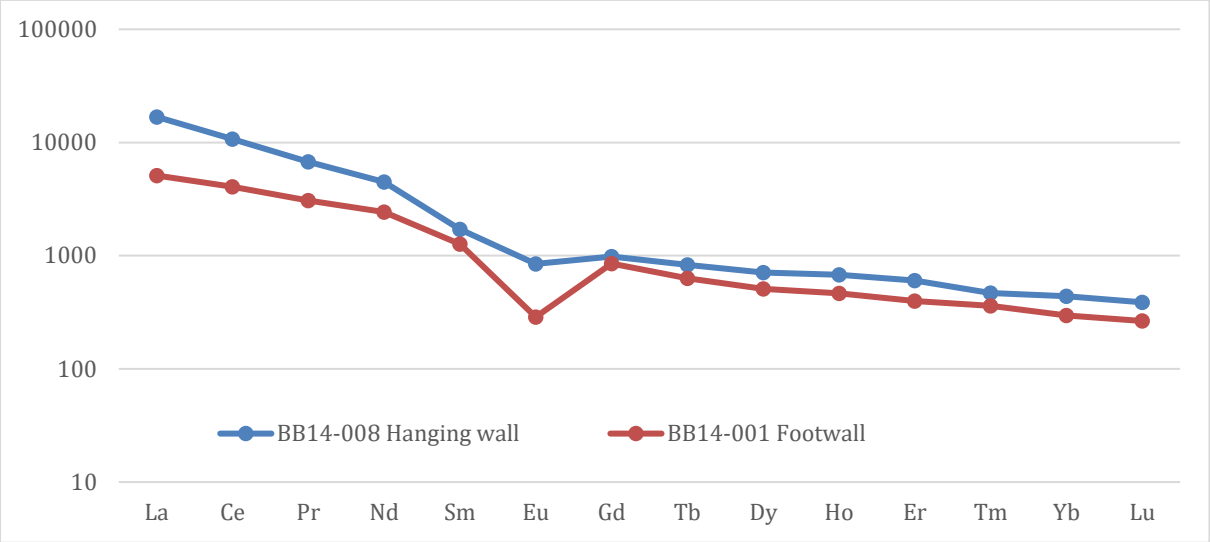

Figure 22. Diagram of the chondrite normalised REE profile in sections BB_14-008 and BB_14-001.

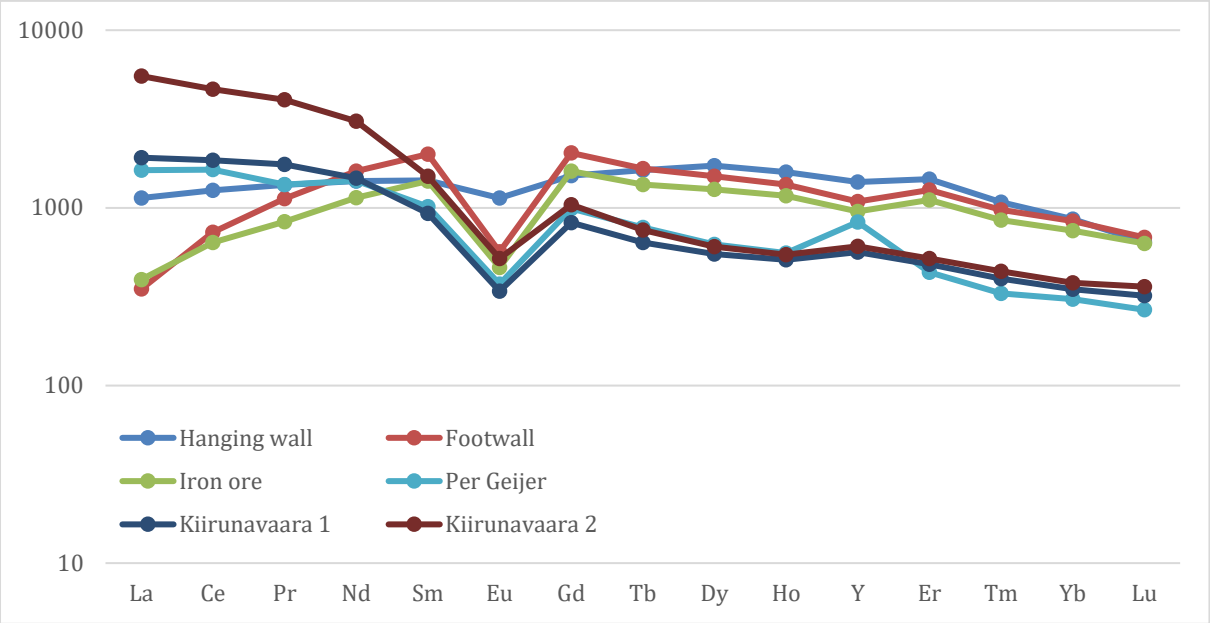

Figure 23. Average chondrite-normalised apatite REE patterns from this study (n = 50), compared to averages from samples KUJ-4, bright and dark apatite from Kiirunavaara (Harlov et al., 2002), and samples from Per Geijer (Lindbom, 2016).

Figure 23 shows the plotted results for the apatite analysis. As previously seen, the apatite in the footwall and iron ore of Blötberget is depleted in LREE compared to the apatite in the hanging wall and other Kiruna-type deposits, such as Posht-e-Badam in Iran and Kiirunavaara in northern Sweden. This depletion is likely due to the early removal of REEs into allanite in the footwall and monazite in the ore zone, both of which strongly incorporate LREE during early crystallisation. In contrast, apatite in the hanging wall exhibits a significantly higher LREE content, nearly an order of magnitude higher, indicating a vastly different mineral assemblage and REE behaviour between the zones. These differences suggest that the footwall and hanging wall formed from separate magmatic batches, with one likely intrusive and the other subvolcanic or extrusive. Apatite from the Blötberget deposit exhibits low concentrations of thorium (Th) and uranium (U), ranging from <1 to 3.31 ppm (average 0.56 ppm) for thorium and <1 to 22.5 ppm (average 3.10 ppm) for uranium. These concentrations show only minor variations across the iron ore, footwall, and hanging wall. Moreover, these Th and U values are significantly lower than those typically reported for well-known Kiruna-type IOA deposits, including the Per Geijer deposit (Lindbom, 2016), and are generally lower than values characteristic of most IOA systems worldwide (Altschuler et al., 1967; Belousova et al., 2002b) The exceptionally low Th and U concentrations observed, particularly within the iron ore, can be primarily attributed to the presence of discrete grains of accessory minerals such as uraninite and thorite, which are highly efficient at sequestering Th and U, thus limiting the availability of these elements for incorporation into the crystal lattice of co-precipitating apatite (Overstreet, 1967). Similarly, in the hanging wall, the low thorium content is likely a consequence of the occurrence of monazite, a phosphate mineral known for its strong affinity for thorium and rare earth elements, often forming as Monazite-(Th). Its presence effectively acts as a sink for Th, preventing it from being incorporated by apatite (Harlov et al., 2002).
While the footwall remains relatively Th-poor when compared to documented literature values for similar deposits (Belousova et al., 2002b). It contains approximately twice the thorium concentration of the iron ore and hanging wall. This enrichment might suggest a comparatively lower abundance of monazite in this specific part of the system, allowing for a slightly greater partitioning of thorium into apatite.

In contrast to the low Th and U concentrations in Blötberget apatites, which range from 5.47 to 6.92 ppm. Furthermore, arsenic (As) concentrations in Blötberget apatite are remarkably low, ranging from 47.8 ppm to 87.3 ppm. This is in stark contrast to the significantly higher arsenic levels typically found in apatite from Per Geijer (200–400 ppm) (Lindbom, 2016), other Kiruna-type deposits (averaging 1205 ppm), and general IOA systems (averaging 768 ppm) (Belousova et al., 2002b; Eklöf et al., 2016). Such depleted arsenic concentrations further distinguish the Blötberget deposit and may indicate different fluid compositions or crystallisation conditions during its formation compared to other well-studied IOA and Kiruna-type systems (Bertil Pålsson & Martinsson et al., 2014) These differences in deleterious elements highlight a unique geochemical signature in Blötberget apatites compared to their regional and typological counterparts (Seydoux-Guillaume et al., 2002).

	As	**Th**	**U**
FW	47,8	0,81	2,89
HW	96,2	0,47	2,19
IO	87,3	0,42	3,60
Per Geijer	200-400	17	1,90
Kiruna-type	1205	196	8,90
Iron ore	768	75	12

Table 14. Average of concentrations of As, Th, and U (ppm) in apatite from Per Geijer (Lindbom, 2016)Kiruna-type deposits (Mao et al., 2016), and iron ore apatite from Durango, Kiruna, and Vestfjord (Belousova et al., 2002b).

4.2.3 Monazite, xenotime, allanite, and others

Monazite grains from both footwall and hanging wall samples show more substantial HREE enrichment than those from the iron ore and Kiirunavaara in Figure 24 (Wanhainen et al., 2017). The weaker Eu anomalies in hanging wall monazites mirror those in apatite, highlighting a similar origin. This supports a model where REE patterns in phosphate minerals are primarily inherited from the local environment rather than an external source. Xenotime, found mainly in the iron ore (IO3) and hanging wall (HW7), shows consistent depletion in LREE and enrichment in MREE-HREE as seen in Figure 25. Compared to Kiruna-type deposits in the Bafq District of Iran, Blötberget shows weaker Eu anomalies and less pronounced Gd–Ho depletion, which is consistent with results suggesting a distinct melt composition and differentiation history (Stosch et al., 2011). LA-ICP-MS REE spider diagrams for allanite are consistent with published data, such as from Grängesberg (Jonsson et al., 2016), supporting their validity. Allanites from the footwall and iron ore are LREE-rich and exhibit strong Eu anomalies, with REE trends similar to those observed in Grängesberg, as shown in Figure 26. The FW2 and IO9 samples, however, are depleted in HREE, which may reflect fluid-mediated alteration or crystallisation from a different, less evolved melt batch.

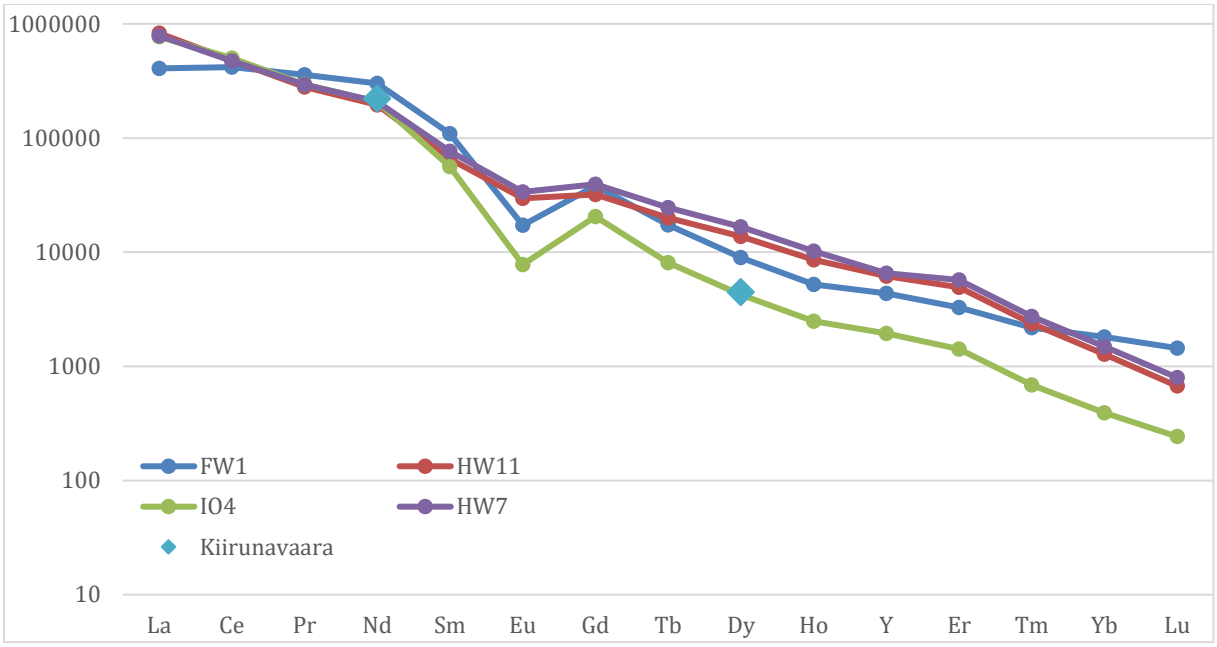

Figure 24. Average chondrite-normalised REE patterns of monazite from this study (n = 18) and from Kiirunavaara (Wanhainen et al., 2017).

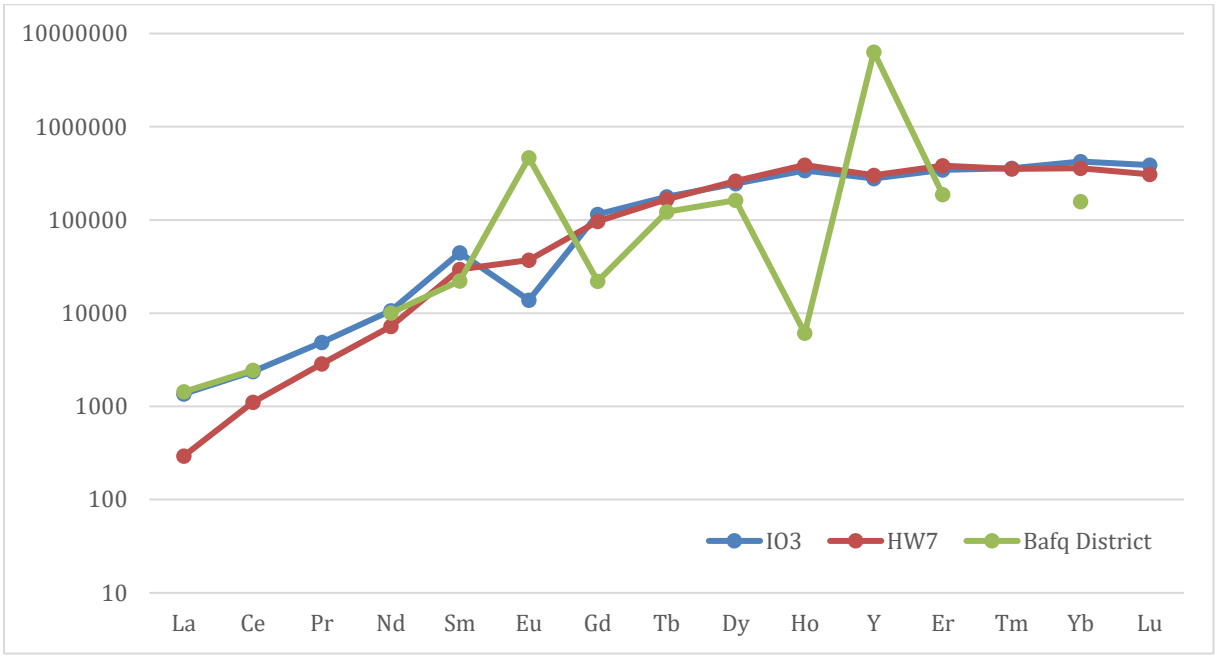

Figure 25. Average chondrite-normalised REE patterns of xenotime from different samples of this study and the Bafq District, East-Central Iran (Stosch et al., 2011).

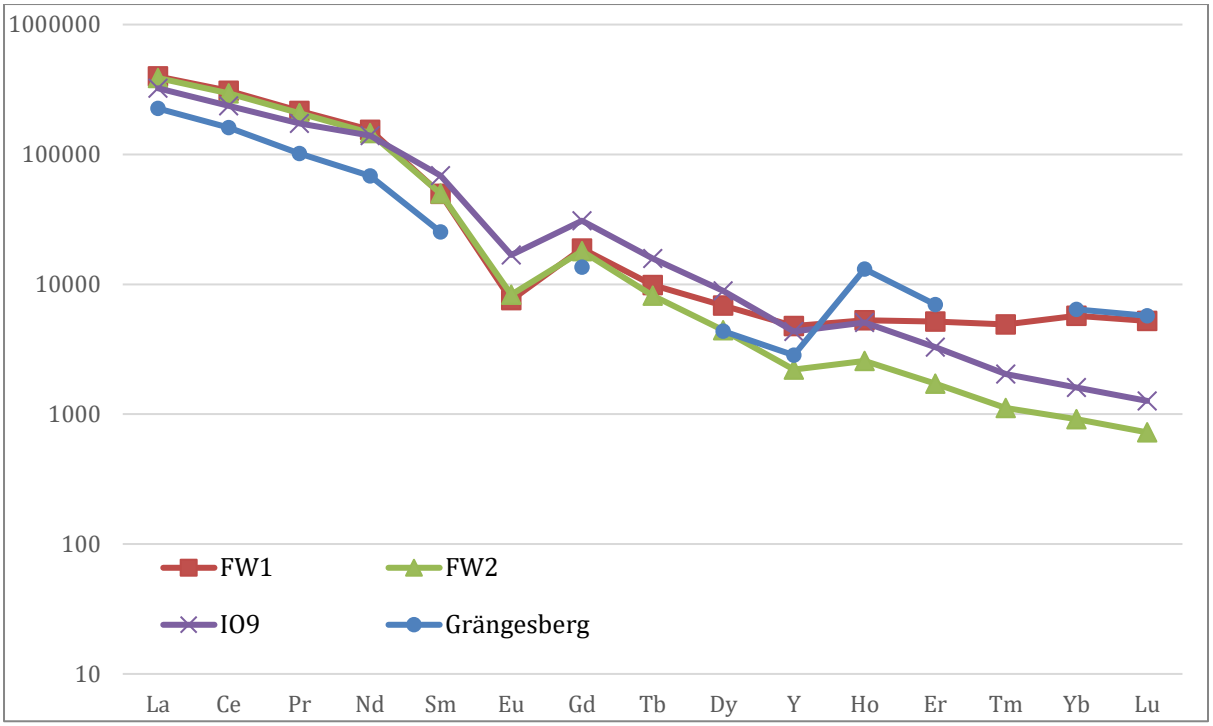

Figure 26. Average chondrite-normalised REE patterns of allanite from different samples from this study compared to Grängesberg (Jonsson et al., 2016).

4.2.4 As, U, Th in monazite and xenotime

Monazite grains of IOA origin are known to have very low Th and U abundances (Harlov et al., 2002). Table 15 of this study shows that the average monazite in the footwall and hanging wall is highly depleted in uranium (61–253 ppm) and thorium (18–1,758 ppm) compared to typical monazite. Iron ore monazite has higher concentrations (Th: 18,000 ppm; U: 10,000 ppm), which align with the lower range of usual values (Belousova et al., 2002b; Budzyń et al., 2017). Table 16 shows that the xenotime in the hanging wall of this Kiruna-type IOA deposit is highly depleted in uranium (20–221 ppm) and thorium (123–555 ppm). In contrast, iron ore xenotime exhibits significantly higher concentrations: uranium (7,200–8,100 ppm) and thorium (13,800–18,400 ppm). Table 17 shows that the allanite in the footwall exhibits U (17–267 ppm) and Th (214–2,729 ppm) concentrations, with similar iron ore values: U (119–267 ppm) and Th (773–1,676 ppm). In contrast, samples from IOA show significantly lower concentrations: uranium (2.7–142 ppm) and thorium (1.9–396 ppm).

Monazite	**As**	**Th**	**U**
FW1	65,7	336	253
HW11	143,9	1291,3	99,7
HW7	292,5	820,4	139,4
IO4	462,6	18895	593

Table 15. Monazite values of Th and U, in ppm, for the iron ore, hanging wall and footwall.

Xenotime	**As**	**Th**	**U**
IO3	146,7	16523,0	7739,0
HW7	292,5	820,4	139,4
IO4	462,6	18895	593

Table 16. Xenotime values of As, Th, and U, in ppm, for iron ore and hanging wall.

Allanite	**As**	**Th**	**U**
FW1	132,1	1744,3	84
FW2	126,9	1485,3	137,7
IO9	125,3	1146,1	192,5

Table 17. Allanite values of As, Th, and U, in ppm, for iron ore and footwall.

4.2.5 Other phases (Samarskite)

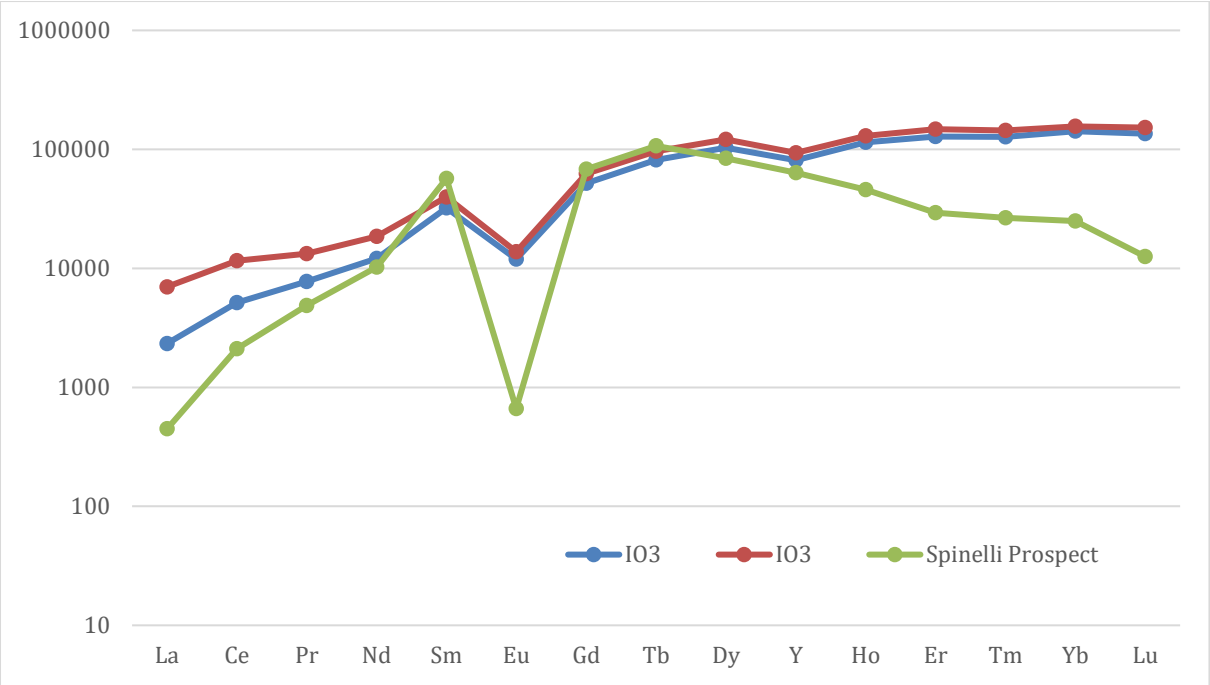

Figure 27. Average chondrite-normalised REE patterns of samarskite from this study (n = 2). Only one sample (IO3) contained samarskite grains. Since no comparable data from Kiruna-type deposits is available, an analysis of the Spinelli Prospect in Glastonbury, Connecticut (Davis & Nicolescu, 2011) was used for comparison.

Samarskite is a rare mineral found only before in some pegmatites around Grängesberg (Erik Jonsson, no publication). This is the first time it was identified in the Blötberget deposit. It shows high enrichment in both LREE and HREE compared to the Spinelli deposit, as displayed in Figure 27 (Lumpkin & Ewing, 1995), likely due to differences in host lithologies and fluid evolution. Trace element data for samarskite remains limited, making comparisons between deposits difficult. Samarskite is typically a Nb-Ta oxide found in granitic pegmatites, not in classic IOA systems. (Černý et al., 1985; Wise et al., 2022). Most occurrences are documented in pegmatites, such as those in the Ånneröd District, Norway, and Ishikawa, Japan. The presence of samarskite in the iron ore is unusual and is not further investigated in this work. Regular bastnäsite and fluocerite grains were also observed along faults, but their small size and irregular, often elongated shapes along fractures prevented analysis by LA-ICP-MS. Their quantities were too low to make a significant contribution to the bulk rock composition.

4.2.6 Comparison of the Blötberget deposit with Grängesberg and other Kiruna-type deposits

The Blötberget deposit can be compared to other IOAs for its main characteristics and is similar to Kiruna-type ones such as those from the Bafq district, Malmberget, and Kiirunavaara. Its

composition is most similar to the Bafq district and Per Geijer, with Cl-poor apatite that was fluid-altered during formation (Lindbom, 2016; Stosch et al., 2011), fluorine as the dominant anion, whereas Kiirunavaara apatites exhibit high Cl contents, up to 0.8 wt% (Martinsson et al., 2012). The fluorapatite contains inclusions of monazite, xenotime, and allanite, similar to those found in Grängesberg (Jonsson et al., 2016). REE minerals are usually found as individual grains or inclusions across different Kiruna-type IOAs, such as monazite, xenotime, and REE-fluorocarbonates. Allanite also occurs in the footwall and inside the ore itself in the Bafq district (Stosch et al., 2011). In contrast, the Kiirunavaara allanites mostly occur in the side rock (Wanhainen et al., 2017). In Blötberget, monazite incorporates significant thorium due to coupled substitution mechanisms (Spear & Pyle, 2002). making it both a valuable REE carrier and a radiogenic phase that must be considered in beneficiation. Phosphorus is elevated due to the presence of abundant fluorapatite, as seen in Per Geijer and Grängesberg (Jonsson et al., 2016; Lindbom, 2016), while sulfur, uranium, arsenic, and fluorine occur at lower levels compared to Kiruna or Bafq, giving Blötberget a relatively cleaner gangue mineralogy. An important feature in Blötberget is the presence of secondary monazite and xenotime, which texturally appear younger than apatite. This resembles observations from Kiruna, with multiple hydrothermal overprints recorded in secondary monazite and xenotime. There, U–Pb ages show crystallisation events at around 1.9 Ga, 1.8–1.7 Ga, and even younger at around 1.5 Ga, indicating that REE-bearing minerals formed long after the main ore stage. Similarly, it could be expected that Blötberget may also record a prolonged or episodic hydrothermal history, where monazite and xenotime crystallised during later fluid activity rather than during the main ore-forming event (Ulf B Andersson et al., 2016).

4.2.7 Formation differences in the Blötberget deposit

Bulk rock Eu/Eu* ratios show a systematic trend: the footwall sample BB_14-001 has a low Eu/Eu* of 0.28, ore zone samples average around 0.31, while BB_14-008 has 0.66, and the hanging wall reaches up to 0.77. This trend is consistent with plagioclase fractionation before emplacement. Eu^{2+} is preferentially incorporated into plagioclase under reducing conditions. Its removal from the melt results in negative Eu anomalies. The low Eu/Eu* values in the footwall and ore zone reflect early and significant plagioclase crystallisation, while the higher values in the hanging wall suggest limited plagioclase fractionation. The presence of these anomalies suggests that plagioclase was removed from the melt before final emplacement, likely due to settling in a staging magma chamber. These differences can be observed when examining the samples from the SEM. Even though the operator biases the analyses, there is an apparent depletion of plagioclase in the footwall and iron ore zones. Therefore, the differences are best explained by early magmatic differentiation and not by post-magmatic fluid overprinting. The REE patterns, especially the Eu anomalies, support the interpretation that these zones did not originate from a single, evolving magma body, but rather from distinct magmas with different compositions emplaced during separate events. The footwall likely formed from a more evolved felsic intrusive rock, possibly granodiorite, while the hanging wall was derived from a less evolved, mafic to intermediate composition, such as a diorite or subvolcanic equivalent. This is further demonstrated by the variation in grain size, with finer-grained rocks in the hanging wall and medium-grained textures in the footwall. The finer-grained unit likely represents a shallow-level subvolcanic or even extrusive facies, whereas the coarser texture in the footwall suggests a deeper-seated intrusive body. This contrast in texture not only reflects differences in emplacement depth but also suggests a different timing, with the intrusive phase cutting into older crust. This interpretation aligns well with the distinct geochemical signatures observed. The presence of allanite in the footwall does not contradict the theory of an evolved magma. Allanite stability is influenced by calcium and fluid

availability, and experimental and natural studies (Janots et al., 2007; Spear & Pyle, 2010) show that allanite can crystallise or reprecipitate during fluid-mediated alteration, even in evolved rocks. While the REE partitioning and Eu anomalies reflect original melt evolution, the presence of allanite could be evidence for later localised fluid-rock interaction. Textural evidence further shows that monazite is never overprinted by apatite, whereas apatite may break down to form monazite. This implies that monazite crystallised later, under cooler conditions, consistent with remobilisation of REE into new phases. Chemically and mineralogically, monazite-rich zones of host rock show significant enrichment, suggesting at least partial redistribution of REE after the main ore stage. Whether this reflects two separate hydrothermal events or one prolonged event spanning a wide temperature range cannot be determined with current data. By comparison, Kiruna records multiple pulses of hydrothermal activity (Ulf B Andersson et al., 2016), and if Blötberget followed a similar trajectory, U–Pb dating of monazite and xenotime might reveal ages between ~1.8 and 1.85 Ga, with the possibility of younger overprints. The most cautious interpretation is that Blötberget experienced a prolonged hydrothermal event, initiated during the waning stages of magmatism, which later redistributed REE and crystallised monazite and xenotime locally in the host rock.

5. Conclusion

This study of the Blötberget deposit highlights major contrasts in REE mineralisation between the footwall and hanging wall. The footwall is dominated by allanite and LREE-depleted apatite with strong negative Eu anomalies, reflecting an evolved intrusive protolith and early plagioclase fractionation. In contrast, the hanging wall contains free-milling monazite and xenotime, as well as apatite enriched in both LREE and HREE with higher Eu/Eu*, consistent with a less evolved, subvolcanic protolith. These differences demonstrate that the two zones represent separate magma batches rather than a single evolving system. Textural evidence shows that monazite postdates apatite, supporting REE remobilisation during a late magmatic to hydrothermal stage. By analogy with Kiruna, where secondary monazite and xenotime formed during multiple hydrothermal pulses between ~1.9 and 1.5 Ga, Blötberget may also record a prolonged or episodic hydrothermal history. This late redistribution locally concentrated REE in the host rocks without overprinting the magmatic signature. Economically, the hanging wall offers more favourable conditions for REE extraction due to free-milling monazite and xenotime, whereas the allanite-rich footwall presents processing challenges. Overall, the REE enrichment at Blötberget reflects the interplay of distinct magmatic sources and later hydrothermal modification. The system is more complex than a simple ore–host contrast, with contrasting mineral assemblages and geochemical signatures in the hanging wall and footwall. Further geochronological dating of monazite and xenotime is needed to establish the precise timing of enrichment relative to iron ore formation.

6. References

A. Lindberg. (2023, January 12). *Europe's largest deposit of rare earth metals located in Kiruna*. https://lkab.com/en/press/europes-largest-deposit-of-rare-earth-metals-is-located-in-the-kiruna-area/

Altschuler, Z. S., Berman, S., & Cuttitta, F. (1967). Rare earths in phosphorites--geochemistry and potential recovery. *U.S. Geol. Surv.,*.

Andersson, U. B., Högdahl, K., Sjöstrom, H., & Bergman, S. (2006). Multistage growth and reworking of the Palaeoproterozoic crust in the Bergslagen area, southern Sweden: evidence from U–Pb geochronology. *Geological Magazine*, *143*(5), 679–697. https://doi.org/10.1017/S0016756806002494

Belousova, E. A., Griffin, W. L., O'Reilly, S. Y., & Fisher, N. I. (2002a). Apatite as an indicator mineral for mineral exploration: trace-element compositions and their relationship to host rock type. *Elsevier*, *76*(1), 45–69. https://doi.org/10.1016/S0375-6742(02)00204-2

Belousova, E. A., Griffin, W. L., O'Reilly, S. Y., & Fisher, N. I. (2002b). Apatite as an indicator mineral for mineral exploration: trace-element compositions and their relationship to host rock type. *Journal of Geochemical Exploration*, *76*(1), 45–69. https://doi.org/10.1016/S0375-6742(02)00204-2

Bertil Pålsson, & Martinsson et al. (2014). Unlocking rare earth elements from European apatite-iron ores. *ERES 2014 - on European Rare Earth Resources 1st International Conference*.

Bonyadi, Z., Davidson, G. J., Mehrabi, B., Meffre, S., & Ghazban, F. (2011). Significance of apatite REE depletion and monazite inclusions in the brecciated Se–Chahun iron oxide–apatite deposit, Bafq district, Iran: Insights from paragenesis and geochemistry. *Chemical Geology*, *281*(3–4), 253–269. https://doi.org/10.1016/j.chemgeo.2010.12.013

Borst, A. M., Smith, M. P., Finch, A. A., Estrade, G., Villanova-de-Benavent, C., Nason, P., Marquis, E., Horsburgh, N. J., Goodenough, K. M., Xu, C., Kynický, J., & Geraki, K. (2020). Adsorption of rare earth elements in regolith-hosted clay deposits. *Nature Communications*, *11*(1), 4386. https://doi.org/10.1038/s41467-020-17801-5

Budzyń, B., Harlov, D. E., Kozub-Budzyń, G. A., & Majka, J. (2017). Experimental constraints on the relative stabilities of the two systems monazite-(Ce) – allanite-(Ce) – fluorapatite and xenotime-(Y) – (Y,HREE)-rich epidote – (Y,HREE)-rich fluorapatite, in high Ca and Na-Ca environments under P-T conditions of 200–1000 MPa and 450–750 °C. *Mineralogy and Petrology*, *111*(2), 183–217. https://doi.org/10.1007/s00710-016-0464-0

Černý, P., Baptista, A., & Cassedanne, J. P. (1985). Zircon hafnifère, samarskite et columbrite d'une pegmatite du Rio Doce, Minas Gerais, Bresil. *The Canadian Mineralogist*, *23*(4), 563–567.

Chalmers Ventures. (2018, May 28). *Minalyze gör storaffär och säljer världsledande instrument för digitalisering av borrkärnor*. Https://Www.Mynewsdesk.Com/Se/Chalmers-Ventures/Pressreleases/Minalyze-Goer-Storaffaer-Och-Saeljer-Vaerldsledande-Instrument-Foer-Digitalisering-Av-Borrkaernor-2519209.

Chen, W., Honghui, H., Bai, T., & Jiang, S. (2017). Geochemistry of Monazite within Carbonatite Related REE Deposits. *Resources*, *6*(4), 51. https://doi.org/10.3390/resources6040051

Davis, F. E., & Nicolescu, S. (2011). Samarskite Rediscovered at the Spinelli Prospect, Glastonbury, Connecticut. *Bulletin of the Peabody Museum of Natural History*, *52*(1), 135–152. https://doi.org/10.3374/014.052.0104

Dostal, J. (2017). Rare Earth Element Deposits of Alkaline Igneous Rocks. *Resources*, *6*(3), 34. https://doi.org/10.3390/resources6030034

Eklöf, S., Högdahl, K., Jonsson, E., & Malehmir, A. (2016). Towards a structural framework for apatite-iron oxide deposits in the Grängesberg-Blötberget area, Bergslagen, Sweden. *32nd Nordic Geologic Winter Meeting*.

Elburg, M., Vroon, P., van der Wagt, B., & Tchalikian, A. (2005). Sr and Pb isotopic composition of five USGS glasses (BHVO-2G, BIR-1G, BCR-2G, TB-1G, NKT-1G). *Chemical Geology*, *223*(4), 196–207. https://doi.org/10.1016/J.CHEMGEO.2005.07.001

European Raw Materials Alliance. (2021, September 30). *Ensuring access to the raw materials for the European Green Deal: A European Call for Action*. https://erma.eu/european-call-for-action/

Eurostat. (2025, April 9). *Imports of rare earth elements saw 30% drop in 2024 - News articles - Eurostat*. https://ec.europa.eu/eurostat/web/products-eurostat-news/w/ddn-20250409-1

Filippelli, G. M. (2008). The Global Phosphorus Cycle: Past, Present, and Future. *Elements*, *4*(2), 89–95. https://doi.org/10.2113/GSELEMENTS.4.2.89

Gadolin, J. (1794). Undersökning af en svart tung stenart ifrån Ytterby stenbrott i Roslagen. *Kungliga Vetenskapsakademiens Handlingar*, *15*, 137–155.

Geijer & Magnusson. (1944). The geology of the Dannemora iron ore deposit, central Sweden. *Sveriges Geologiska Undersökning (SGU)*, 35.

Goodenough, K. M., Schilling, J., Jonsson, E., Kalvig, P., Charles, N., Tuduri, J., Deady, E. A., Sadeghi, M., Schiellerup, H., Müller, A., Bertrand, G., Arvanitidis, N., Eliopoulos, D. G., Shaw, R. A., Thrane, K., & Keulen, N. (2016). Europe's rare earth element resource potential: An overview of REE metallogenetic provinces and their geodynamic setting. *Ore Geology Reviews*, *72*, 838–856. https://doi.org/10.1016/J.OREGEOREV.2015.09.019

Harlov, D. E., Andersson, U. B., Förster, H. J., Nyström, J. O., Dulski, P., & Broman, C. (2002). Apatite–monazite relations in the Kiirunavaara magnetite–apatite ore, northern Sweden. *Chemical Geology*, *191*(1–3), 47–72. https://doi.org/10.1016/S0009-2541(02)00148-1

Henderson, P. (1984). General Geochemical Properties and Abundances of the Rare Earth Elements. *Rare Earth Element Geochemistry*, *2*, 1–32. https://doi.org/10.1016/B978-0-444-42148-7.50006-X

Henriksson, J. S., Troll, V. R., Kooijman, E., Bindeman, I., Naeraa, T., & Bauer, T. E. (2024). Origin and Affinities of the Malmberget Iron Oxide-Apatite Deposit, Northern Sweden: Insights From Magnetite Chemistry and Fe-O Isotopes. *Earth Science, Systems and Society*, *4*(1). https://doi.org/10.3389/esss.2024.10126

Henriksson, J. S., Troll, V. R., Kooijman, E., Bindeman, I., Naeraa, T., Bauer, T. E., Smith, A., Tornos, F., & Yan, S. (2024). Origin and Affinities of the Malmberget Iron Oxide-Apatite Deposit, Northern Sweden: Insights From Magnetite Chemistry and Fe-O Isotopes. *Earth Science, Systems and Society*, *4*(1). https://doi.org/10.3389/ESSS.2024.10126

Hitzman, M. W., Oreskes, N., & Einaudi, M. T. (1992). Geological characteristics and tectonic setting of proterozoic iron oxide (Cu□U□Au□REE) deposits. *Precambrian Research*, *58*(1–4), 241–287. https://doi.org/10.1016/0301-9268(92)90121-4

Hughes, J. M., & Rakovan, J. (2002). The Crystal Structure of Apatite, Ca5(PO4)3(F,OH,Cl). *Reviews in Mineralogy and Geochemistry*, *48*(1), 1–12. https://doi.org/10.2138/rmg.2002.48.1

Hughes, J. M., & Rakovan, J. F. (2015). Structurally Robust, Chemically Diverse: Apatite and Apatite Supergroup Minerals. *Elements*, *11*(3), 165–170. https://doi.org/10.2113/gselements.11.3.165

Intertek. (2025, April 15). *Minalyzer CS fact sheet*. Https://Www.Intertek.Com/Siteassets/Minerals/Intertek-Minerals-Minalyzer-Cs-Fact-Sheet.Pdf.

J. Edwards. (2023, March 1). *Finland Projects — Prospech Limited*. https://prospech.com.au/finland-projects

Jackson, W. D., & Christiansen, G. (1993). *International strategic minerals inventory summary report; rare-earth oxides*. https://doi.org/10.3133/cir930N

Janots, E., Berger, A., & Engi, M. (2011). Physico-chemical control on the REE minerals in chloritoid-grade metasediments from a single outcrop (Central Alps, Switzerland). *Lithos*, *121*(1–4), 1–11. https://doi.org/10.1016/j.lithos.2010.08.023

Janots, E., Brunet, F., Goffé, B., Poinssot, C., Burchard, M., & Cemič, L. (2007). Thermochemistry of monazite-(La) and dissakisite-(La): implications for monazite and allanite stability in metapelites. *Contributions to Mineralogy and Petrology*, *154*(1), 1–14. https://doi.org/10.1007/s00410-006-0176-2

Janots, E., Engi, M., Berger, A., Allaz, J., Schwarz, J. -O., & Spandler, C. (2008). Prograde metamorphic sequence of REE minerals in pelitic rocks of the Central Alps: implications for allanite–monazite–xenotime phase relations from 250 to 610 °C. *Journal of Metamorphic Geology*, *26*(5), 509–526. https://doi.org/10.1111/j.1525-1314.2008.00774.x

Jansson, N. F., & Allen, R. L. (2011). Timing of volcanism, hydrothermal alteration and ore formation at Garpenberg, Bergslagen, Sweden. *GFF*, *133*(1–2), 3–18. https://doi.org/10.1080/11035897.2010.547597

Jiao, J. (2011). *Petrography and geochemistry of a section through the Blötberget apatite-iron oxide deposit, Bergslagen, south central Sweden*. https://www.diva-portal.org/smash/record.jsf?pid=diva2:475539

Jochum, K. P., Weis, U., Stoll, B., Kuzmin, D., Yang, Q., Raczek, I., Jacob, D. E., Stracke, A., Birbaum, K., Frick, D. A., Günther, D., & Enzweiler, J. (2011). Determination of reference values for NIST SRM 610–617 glasses following ISO guidelines. *Wiley Online LibraryKP Jochum, U Weis, B Stoll, D Kuzmin, Q Yang, I Raczek, DE Jacob, A Stracke, K BirbaumGeostandards and Geoanalytical Research, 2011•Wiley Online Library*, *35*(4), 397–429. https://doi.org/10.1111/J.1751-908X.2011.00120.X

Jonsson, E., Harlov, D. E., MaJka, J., Högdahl, K., & Persson-Nilsson, K. (2016). Fluorapatite-monazite-allanite relations in the Grängesberg apatite-iron oxide ore district, Bergslagen, Sweden. *American Mineralogist*, *101*(8), 1769–1782. https://doi.org/10.2138/am-2016-5655

Jonsson, E., Troll, V. R., Högdahl, K., Harris, C., Weis, F., Nilsson, K. P., & Skelton, A. (2013). Magmatic origin of giant 'Kiruna-type' apatite-iron-oxide ores in Central Sweden. *Scientific Reports*, *3*(1), 1644. https://doi.org/10.1038/srep01644

Kanazawa, Y., & Kamitani, M. (2006). Rare earth minerals and resources in the world. *Journal of Alloys and Compounds*, *408–412*, 1339–1343. https://doi.org/10.1016/J.JALLCOM.2005.04.033

Khoshnoodi, K., Ziapour, S., Yazdi, M., & Cuney, M. (2023). Mineralogy of various types of Th-U-REE mineralisation in the iron oxide – apatite deposits of the Bafq district, Central Iran. *Applied Earth Science*, *132*(1), 1–15. https://doi.org/10.1080/25726838.2022.2147300

Leading Edge Materials. (2021, July 22). *Leading Edge Materials Announces Positive Preliminary Economic Assessment Results for its Norra Karr REE Project With*

US$1,026M Pre-tax NPV(10%) And 30.8% Pre-tax IRR - Leading Edge Materials Corp. https://leadingedgematerials.com/leading-edge-materials-announces-positive-preliminary-economic-assessment-results-for-its-norra-karr-ree-project-with-us1026m-pre-tax-npv10-and-30-8-pre-tax-irr/

Lindbom, M. (2016). *Trace element geochemistry of apatite from the Per Geijer ores in the Kiruna area, northern Norrbotten, Sweden*. https://urn.kb.se/resolve?urn=urn:nbn:se:ltu:diva-48244

Liu, Y., Hu, Z., Gao, S., Günther, D., Xu, J., Gao, C., & Chen, H. (2008). In situ analysis of major and trace elements of anhydrous minerals by LA-ICP-MS without applying an internal standard. *Chemical Geology*, *257*(1–2), 34–43. https://doi.org/10.1016/j.chemgeo.2008.08.004

Lugo-Zazueta, R. E., Gleadow, A. J. W., Kohn, B. P., Sahu, H., & Bermúdez, M. A. (2024). Apatite Fission-Track Dating: A Comparative Study of Ages Obtained by the Automated Counting LA-ICP-MS and External Detector Methodologies. *Lithosphere*, *2023*(Special 14). https://doi.org/10.2113/2023/lithosphere_2023_260

Lumpkin, G. R., & Ewing, R. C. (1995). Geochemical alteration of pyrochlore group minerals; pyrochlore subgroup. *American Mineralogist*, *80*(7–8), 732–743. https://doi.org/10.2138/am-1995-7-810

Magnusson, N. H. (1970). The origin of the iron ores in Central Sweden and the history of their alterations. *Sveriges Geologiska Undersökning*.

Majka, J., Włodek, A., Jonsson, E., & Högdahl, K. (2022). Contrasting coronas: microscale fluid variation deduced from monazite breakdown products in altered metavolcanic rocks associated with the Grängesberg apatite-iron oxide ore, Bergslagen, Sweden. *GFF*, *144*(2), 89–96. https://doi.org/10.1080/11035897.2022.2083224

Mao, M., Rukhlov, A. S., Rowins, S. M., Spence, J., & Coogan, L. A. (2016). Apatite trace element compositions: A robust new tool for mineral exploration. *Pubs.Geoscienceworld.OrgM Mao, AS Rukhlov, SM Rowins, J Spence, LA CooganEconomic Geology, 2016•pubs.Geoscienceworld.Org*, *111*, 1187–1222. https://pubs.geoscienceworld.org/segweb/economicgeology/article-abstract/111/5/1187/152473

Martinsson, O., Öberg, E., & Fredriksson, A. (2012). Apatite for Extraction – Mineralogy of Apatite and REE in the Kiirunavaara Fe-deposit. *Proceedings of the XXVI International Mineral Processing Congress*, 3287–3297.

McDonough, W. F., & Sun, S. s. (1995). The composition of the Earth. *Chemical Geology*, *120*(3–4), 223–253. https://doi.org/10.1016/0009-2541(94)00140-4

Moldoveanu, G. A., & Papangelakis, V. G. (2016). An overview of rare-earth recovery by ion-exchange leaching from ion-adsorption clays of various origins. *Mineralogical Magazine*, *80*(1), 63–76. https://doi.org/10.1180/minmag.2016.080.051

Nesse, W. D. (2023). *Introduction to mineralogy* (Oxford: Oxford University Press, Ed.; 4th ed).

Nordic Iron. (2023, November 14). *Continued positive results concerning rare earth elements at Blötberget*. https://storage.mfn.se/8c893299-1a8a-432f-936b-63634473ea5d/continued-positive-results-concerning-rare-earth-elements-at-blotberget.pdf

Nordic Iron. (2025). *Blötberget - Nordic Iron*. https://nordiciron.se/en/verksamhet/vara-omraden/blotberget/

Nystroem, J. O., & Henriquez, F. (1994). Magmatic features of iron ores of the Kiruna type in Chile and Sweden; ore textures and magnetite geochemistry. *Economic Geology*, *89*(4), 820–839. https://doi.org/10.2113/gsecongeo.89.4.820

Overstreet, W. C. (1967). *The geologic occurrence of monazite*. https://doi.org/10.3133/pp530

Pan, Y., & Fleet, M. E. (2002). Compositions of the Apatite-Group Minerals: Substitution Mechanisms and Controlling Factors. *Reviews in Mineralogy and Geochemistry*, *48*(1), 13–49. https://doi.org/10.2138/rmg.2002.48.2

Parak, T. (1975). Kiruna iron ores are not "intrusive-magmatic ores of the Kiruna type." *Economic Geology*, *70*(7), 1242–1258. https://doi.org/10.2113/gsecongeo.70.7.1242

Piccoli, P. M., & Candela, P. A. (2002). Apatite in Igneous Systems. *Reviews in Mineralogy and Geochemistry*, *48*(1), 255–292. https://doi.org/10.2138/rmg.2002.48.6

Ptáček, P. (2016). *Apatites and their Synthetic Analogues - Synthesis, Structure, Properties and Applications*. InTech. https://doi.org/10.5772/59882

Rasool, M. H., Ridha, S., Ahmad, M., Shamsuddun, R. A. B., Zahoor, M. K., & Khan, A. (2025). A Mineralogical Perspective on Rare Earth Elements (REEs) Extraction from Drill Cuttings: A Review. *Minerals*, *15*(5), 533. https://doi.org/10.3390/min15050533

Reich, M., Simon, A. C., Barra, F., Palma, G., Hou, T., & Bilenker, L. D. (2022). Formation of iron oxide–apatite deposits. *Nature Reviews Earth & Environment*, *3*(11), 758–775. https://doi.org/10.1038/s43017-022-00335-3

Renas Sidahmed. (2023, June 15). *Wind turbines drive REE pricing not EVs*. https://acfequityresearch.com/wind-turbines-drive-ree-pricing-not-evs/?utm_source=chatgpt.com

Rojas, P. A., Barra, F., Deditius, A., Reich, M., Simon, A., Roberts, M., & Rojo, M. (2018). New contributions to the understanding of Kiruna-type iron oxide-apatite deposits revealed by magnetite ore and gangue mineral geochemistry at the El Romeral deposit, Chile. *Ore Geology Reviews*, *93*, 413–435. https://doi.org/10.1016/j.oregeorev.2018.01.003

Rønsbo, J. G. (2008). Apatite in the Ilímaussaq alkaline complex: Occurrence, zonation and compositional variation. *Lithos*, *106*(1–2), 71–82. https://doi.org/10.1016/j.lithos.2008.06.006

Shannon, R. D. (1976). Revised effective ionic radii and systematic studies of interatomic distances in halides and chalcogenides. *Acta Crystallographica Section A*, *32*(5), 751–767. https://doi.org/10.1107/S0567739476001551

Shannon, R. D., & Prewitt, C. T. (1969). Effective ionic radii in oxides and fluorides. *Acta Crystallographica Section B Structural Crystallography and Crystal Chemistry*, *25*(5), 925–946. https://doi.org/10.1107/S0567740869003220

Spear, F. S., & Pyle, J. M. (2002). Apatite, Monazite, and Xenotime in Metamorphic Rocks. *Reviews in Mineralogy and Geochemistry*, *48*(1), 293–335. https://doi.org/10.2138/rmg.2002.48.7

Spear, F. S., & Pyle, J. M. (2010). Theoretical modeling of monazite growth in a low-Ca metapelite. *ElsevierFS Spear, JM PyleChemical Geology, 2010•Elsevier*, *273*(1–2), 111–119. https://doi.org/10.1016/J.CHEMGEO.2010.02.016

Stephens, M. B., Ripa, M., Lundström, I., Persson, L., Bergman, T., Ahl, M., & Bergström, U. (2009). Synthesis of the bedrock geology in the Bergslagen region, Fennoscandian Shield, south-central Sweden. *Geological Survey of Sweden*, *58*, 259.

Stephens, M., & Jansson, N. (2020). *Sweden: Lithotectonic framework, tectonic evolution and mineral resources*. https://doi.org/10.1144/M50-2018-30

Stosch, H. G., Romer, R. L., Daliran, F., & Rhede, D. (2011). Uranium–lead ages of apatite from iron oxide ores of the Bafq District, East-Central Iran. *SpringerHG Stosch, RL Romer, F Daliran, D RhedeMineralium Deposita, 2011•Springer*, *46*(1), 9–21. https://doi.org/10.1007/S00126-010-0309-4

Strategic Metals Invest. (2025). *Greenland's Rare Earths - Deep Dive into What Lies Beneath*. Https://Strategicmetalsinvest.Com/Greenland-Rare-Earths-Deep-Dive-2025/.

Tegengren, F. R. (1924). *Sveriges ädlare malmer och bergverk*.

Troll, V. R., Weis, F. A., Jonsson, E., Andersson, U. B., Majidi, S. A., Högdahl, K., Harris, C., Millet, M.-A., Chinnasamy, S. S., Kooijman, E., & Nilsson, K. P. (2019). Global Fe–O isotope correlation reveals magmatic origin of Kiruna-type apatite-iron-oxide ores. *Nature Communications*, *10*(1), 1712. https://doi.org/10.1038/s41467-019-09244-4

Ulf B Andersson, Thomas Zack, K Aupers, H Blomgren, Johan Hogmalm, Bernhard Schulz, & J. Krause. (2016). Ages of hydrothermal overprints in the Kiruna iron oxide-apatite ores as recorded in secondary monazite and xenotime. *International Geological Congress*, *3431*.

Urbain, G. (1907). Les terres rares. Lutécium, nouveau métal. *Comptes Rendus Hebdomadaires Des Séances de l'Académie Des Sciences*, *145*, 759–762.

U.S. Geological Survey. (2025). *Mineral commodity summaries 2025*. https://doi.org/10.3133/mcs2025

Wang, Y., Zhu, X., Tang, C., Mao, J., & Chang, Z. (2021). Discriminate between magmatic- and magmatic-hydrothermal ore deposits using Fe isotopes. *Ore Geology Reviews*, *130*, 103946. https://doi.org/10.1016/j.oregeorev.2020.103946

Wanhainen, C., Palsson, B. I., Martinsson, O., & Lahaye, Y. (2017). Rare earth mineralogy in tailings from Kiirunavaara iron ore, northern Sweden: Implications for mineral processing. *SpringerC Wanhainen, BI Pålsson, O Martinsson, Y LahayeMinerals & Metallurgical Processing, 2017•Springer*, *34*(4), 189–200. https://doi.org/10.19150/MMP.7859

Weeks, M. E., & Leicester, H. M. (1968). Discovery of the Elements. *Easton: Journal of Chemical Education*, *7*.

Windfakten. (2024). Rare Earths in the Wind Industry. In *Windfakten Report*. Windfakten.

Wise, M. A., Müller, A., & Simmons, W. B. (2022). A proposed new mineralogical classification system for granitic pegmatites. *The Canadian Mineralogist*, *60*(2), 229–248. https://doi.org/10.3749/canmin.1800006